
Numerical methods for computation of flow around road vehicles

Syed R. Ahmed

13.1 Introduction

The traditional predictive tools used in the automobile industry to evaluate aerodynamic performance are the wind tunnel and road tests. Full-scale vehicle wind tunnels are expensive to build and operate whereas scale model test results are subject to numerous doubts associated with realistic simulation of Reynolds number, surface and underbody details, engine cooling and passenger compartment flows, tunnel wall boundary layer and model support interference effects, model and wake blockage effects, effects of flow-intrusive probes, etc.

Road tests represent the most realistic simulation of the environment in which a vehicle operates. However, the difficulties associated with the ever-changing environment often make the results obtained open to debate. Great care is needed to make the results meaningful and conclusive.

Computers, and with them computational fluid dynamics (CFD), are slowly emerging as additional basic tools in aerodynamic design. Wind tunnels and computers are both simulators—wind tunnels analogue, computers digital. Their characteristic differences make them complementary rather than directly competitive. The relative role of the two simulation techniques is however changing.

In future, wind tunnels may be used more for validation and refinement of theoretical predictions or global simulation of the entire flow field rather than for extensive parameter studies as in the past.

Numerical simulation is well suited to the analysis of a wide range of shape options—for example during an early design stage—thus increasing the prospect that an optimum shape will be identified. Sometimes a numerical simulation permits the investigation of situations that cannot be realistically duplicated in a wind tunnel. The aerodynamics of two vehicles in the passing or overtaking mode, for example, poses a difficult problem for wind tunnel tests.

Numerical simulations are most useful in predicting trends of how shape changes will affect flow field features. Absolute performance value prediction is usually poor. Computer size and speed limitations, and the lack of information about the physics involved, often limit the predictive capacity of numerical methods.

An interesting application of numerical methods is the effectivity enhancement of wind tunnel tests through pre-test planning, on-line test diagnosis and post-test validation. Although this may not lead to a reduction in wind tunnel testing, it can help to ensure that the time spent is used more intelligently.

All numerical methods to compute fluid flow are based on approximations to the full Navier-Stokes equations. These are second order non-linear partial differential equations which govern all fluid motion. Except for the simplest approximations, they are solved by techniques such as finite element, finite volume or finite difference to achieve the spatial and temporal detail needed.

In these techniques the physical region of interest is divided up (or discretized) by a two- or three-dimensional grid. Such grids are in practice complicated orthogonal or non-orthogonal networks that may originate from the body contour envelope and have a flow physics oriented spacing. The vast amount of detail needed to analyse the flow around a real vehicle will limit the use of computational methods for quite some time to come. Only flow simulation around basic vehicle-like configurations appears to be feasible at present.

Numerical methods to solve the Navier-Stokes equations can be classified into the following four categories, depending on the degree of approximation made:

1. Linearized inviscid flow methods
2. Non-linear inviscid flow methods
3. Methods based on Reynolds-averaged Navier-Stokes equations
4. Solutions of full Navier-Stokes equations.

Linearized inviscid flow methods are used routinely in aircraft design and have reached maturity. They are applicable to subsonic, contour-attached flow. Vortex-lattice and panel method codes belong to this category. Use of these methods to compute the flow field around cars, whose predominant feature is the large separation region at vehicle rear, remains severely restricted.

The non-linear inviscid flow methods based on the solution of the Euler equations have established themselves as accurate design tools for the prediction of trans-sonic flow around a class of aircraft components, e.g. wings. The 'automatic' simulation of flow kinematics in the subsonic separated flow computations claimed by developers of these code needs further substantiation. Provided this simulation capability turns out to be general, a coupling of these methods with boundary layer approaches may mean a significant advance also of benefit to vehicle aerodynamicists.

Category three methods, based on the Reynolds-averaged Navier-Stokes equations, are still undergoing extensive research and development. These equations need a turbulence model for closure. The difficulty of modelling turbulence with sufficient generality and the complex mesh generation needed to resolve flows such as those around road vehicles are the principal difficulties that have to be overcome.

Methods to solve the full Navier-Stokes equations, which belong to the last category named above, are practically non-existent. Only very preliminary research is under way here.

In this chapter some current developments in the application of numerical methods to computing the flow around road vehicle-like bodies are mentioned. The choice of the methods treated is conservative. Mostly those approaches have been detailed whose direct applicability to vehicle-type flows has been demonstrated by more than one user in the open literature. Briefer mention is made of methods that have not yet found wider usage but display innovative ideas which may help further development of the first mentioned approaches.

A comprehensive picture of the application of computational fluid dynamics (CFD) to road vehicle flow has to remain incomplete as this technology is in the preliminary stage of emergence. The more modest aim of what follows is to introduce these techniques which bear the promise of developing into a complementary design tool besides the wind tunnel to engineering staff from the automotive industry who have had little experience with CFD in the past.

13.2 Nature of flow around road vehicles

The flow generated by the movement of a road vehicle is extremely complex. In contrast to the flows around aeronautical configurations, the road vehicle flow field is characterized by regions of separation both small and large. These can be of open or closed type and may exhibit quasi-two-dimensional or fully three-dimensional structures.

The smaller regions of local separation occur at body appendages such as headlights, mirrors, door handles, windscreen wipers etc. Large areas of separated flow are present at the trailing perimeter of the vehicle body and on the underside where the flow is disturbed by mechanical and structural elements and by the rotating wheels.

A feature of the environment in which a road vehicle operates is the ambient wind that is almost always present. The speed and path of the vehicle differ from that of the wind. In the resulting yawed flow, the wake and the local regions of separation are asymmetrically deformed, thus adding to the complexity of the flow field. Temporal changes in ambient conditions superimpose a time history on the phenomena in addition to the inherent unsteadiness of separated flows.

Figures 1.6, 4.3 and 4.4 give a schematic impression of the flow separations that may occur at the various locations. As in an actual situation, some or all of the separation phenomena may be present; the flow field is not known *a priori*. Mutual interference of the various separated flow regions, often triggered by minor changes in body geometry, are known to induce abrupt changes of the overall flow field. Air drawn from or exhausted into the external flow for the purpose of engine and brake cooling and ventilation of the passenger compartment links aero-thermodynamically the external flow with these internal flows.

Road vehicles move in close proximity to the ground and share common pathways, so that interaction between the overall flow fields of vehicles of different shape and size during the passing and overtaking phases is a common occurrence.

Flow passing over the vehicle underbody is restricted by the presence of

the ground. Interaction between flows generated by the rough vehicle underbody, wheels and the ground result in a complex viscous flow in this region.

13.3 Some difficulties of numerical simulation of the road vehicle flow field

Computational fluid dynamics, which has established itself as an effective design tool in many aeronautical applications, is based on idealized models of the overall flow. These models possess sufficient generality for their application to a broad range of similar components, for example a wing profile, to be frequently a routine exercise.

The successful abstraction of idealized flow modules from real flow situations in many aeronautical applications is a consequence of the prime requirement to avoid, minimize or control the separation phenomena in these cases. With the shape design margins available to the aeronautical engineer, this is achieved to a good degree, at least for the designed cruise conditions.

With separation then playing a less crucial role, the viscous effects can be hypothesized to act in the immediate vicinity of the body surface, in the so-called 'boundary layer'. Except where this boundary layer separates, its main effect is a particular outward displacement of the 'inviscid' flow away from the body surface. A possibility for numerical simulation of this flow phenomenon caused by viscosity is increasing the local body thickness by an amount equal to the displacement thickness of the boundary layer. This can be done in a 'correction' step performed after computing the inviscid flow.

In this simple example of flow modelling, only one set of governing equations is needed for the single flow module used for the entire flow field. More often a set of flow modules is blended together to simulate the significant part of the flow. Each of these idealized flow modules is then treated with a different approximation of the Navier-Stokes equations.

Regions of separated flow being the key features of a road vehicle flow field, an analytical approach of the type mentioned above is extremely difficult. Even simplified, basic vehicle-like configurations free of all appendages and having smooth surfaces create 'closed' separation regions and a large wake. One of the main difficulties encountered in modelling such flows is the lack of generally applicable information about three-dimensional separated flows. The variety of separation phenomena that can occur in three-dimensional flows is a subject of continuing research. Factors governing the initiation of different types of three-dimensional flow separation, kinematics of the structures in separated flow, unsteady behaviour of bluff body wakes, turbulence, etc., are all phenomena not well understood. Modular or sequential approaches similar to those used in aircraft applications remain inadequate since computational methods to treat three-dimensional boundary layers, in an adverse pressure gradient and strong cross-flow environment, which is typical of road vehicle flows, are not yet available.

As noted earlier, use of Reynolds-averaged Navier-Stokes equations needs a turbulence model to close the system of equations and make them amenable to solution. Standard mixing length and eddy viscosity concepts cannot be used to model complex real turbulent flows. Higher order turbulence models, currently not available, are therefore needed.

13.4 Relative magnitudes of the forces in a flow field

The force on a body arising from its motion relative to a surrounding fluid depends on the geometric shape and orientation of the body and the physical properties of the fluid. In general, it is immaterial whether the fluid moves and the body is stationary or vice versa, provided the nature of relative motion remains identical. In what follows, the body is considered to be stationary and the fluid moves.

For a rigid body, the geometric shape can be characterized by a length l . The orientation is specified by two angles α and β , which the velocity vector V of the fluid forms with a body-centred coordinate system. Road vehicle flow being of interest here, the surrounding fluid, air, is considered to extend over an infinite region. Fluid properties of importance are density ρ , viscosity μ and compressibility.

Considering a fluid element of volume $dx\,dy\,dz = \delta\text{vol}$ in the flow field (Fig. 13.1), the forces acting on the element are the inertial force, gravity force, pressure force and the viscous force.

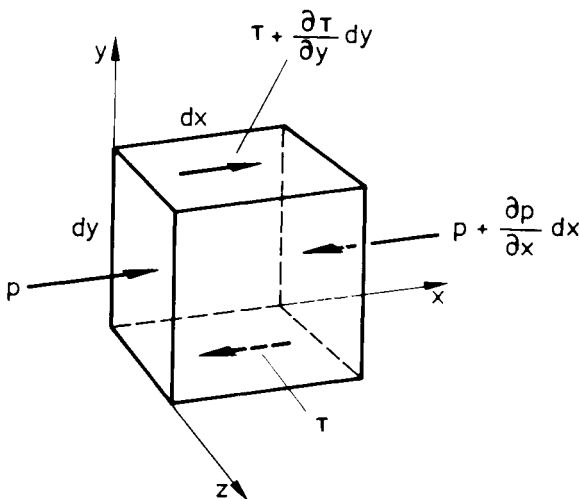


Figure 13.1 Forces acting on a fluid element

The time rate of change of momentum is equal and opposite in sign to the inertial force. The change of momentum of the volume element having a velocity V is proportional to $\rho V \delta\text{vol}$. This change may be assumed to take place in a characteristic time interval; for example, the time needed by the element to traverse a distance equal to the characteristic length l . Inertial force F_i acting on the element is given by the proportionality

$$F_i \sim \frac{\rho V \delta \text{vol}}{l/V} = \frac{\rho V^2 \delta \text{vol}}{l} \quad (13.1)$$

The balance of pressure forces on the opposite faces— dx apart—of the fluid element (Figure 13.1) gives a net pressure force equal to

$$\frac{\partial p}{\partial x} \cdot dx \, dy \, dz = \frac{\partial p}{\partial x} \cdot \delta \text{vol} \quad (13.2)$$

Assuming all components of the pressure force are of same magnitude, the pressure force F_p can be set proportional to

$$F_p \sim \frac{\delta p}{l} \cdot \delta \text{vol} \quad (13.3)$$

Here δp is a ‘representative’ pressure change and the length x in Eqn (13.2) has been replaced by the characteristic length l .

The viscous force can be estimated in a similar manner. Considering only one component acting in the x -direction (Fig. 13.1), the balance of viscous forces acting on the faces— dy apart—of the fluid element delivers a viscous force acting in the x -direction equal to

$$\frac{\partial \tau}{\partial y} \cdot dx \, dy \, dz = \frac{\partial \tau}{\partial y} \cdot \delta \text{vol} \quad (13.4)$$

The shear stress τ , can be expressed in terms of the velocity gradient in the y -direction (see section 2.1.2, Eqn 2.1) as

$$\tau = \mu \cdot \frac{\partial u}{\partial y} \quad (13.5)$$

where μ is the coefficient of viscosity and u the velocity component in the x -direction. Replacing u and y with characteristic quantities V and l and assuming, as earlier, equality in magnitude of all shear force components, it follows

$$\frac{\partial \tau}{\partial y} \delta \text{vol} \sim \mu \frac{V}{l^2} \delta \text{vol} \quad (13.6)$$

The relative magnitudes of the inertial force, pressure force and viscous force acting on the fluid element can be expressed as

$$F_i : F_p : F_v = \frac{\rho V^2}{l} : \frac{\delta p}{l} : \mu \frac{V}{l^2} \quad (13.7)$$

13.5 Criteria for consideration of viscous and compressibility effects in a flow field

The ratio of inertial force to viscous force is a non-dimensional parameter of fundamental importance in fluid mechanics. Called the Reynolds number Re , its value is given by (see Eqn 13.7)

$$Re = \frac{\rho V^2/l}{\mu V/l^2} = \frac{\rho}{\mu} V l = \frac{V l}{\nu} \quad (13.8)$$

where ν denotes the kinematic viscosity μ/ρ . The proportionality

$$Re \sim \frac{\text{inertial force}}{\text{viscous force}} \quad (13.9)$$

enables an estimation of the relative roles that these forces play in a flow regime.

With the average length and maximum speed of current road vehicles, the Reynolds number of the flow field varies between 10^5 and 10^8 . Accordingly, the inertial forces in the major part of the attached flow field are some orders of magnitude larger than the viscous forces. In the immediate vicinity of the body surface the flow is retarded and the velocity on the surface itself reduces to zero ('no slip' condition). In this thin 'boundary layer' region the viscous forces play a key role. The 'thin' boundary layer is a consequence of the low value of the kinematic viscosity of air. Thus the assumption of a 'perfect fluid' behaviour for the flow outside the attached boundary layer represents a good approximation of the real flow.

The decision whether or not compressibility effects in a flow are significant is related to the change in volume effected by the pressure changes due to motion of the fluid. For a perfect gas

$$\frac{\delta p}{p} = - \frac{\delta \text{vol}}{\text{vol}} \quad (13.10)$$

with $\delta p/p$ and $\delta \text{vol}/\text{vol}$ denoting the relative changes in pressure p and volume 'vol'. Using the law of conservation of mass, the relative change in volume can be replaced by the change in density as

$$\frac{\delta p}{p} = \frac{\delta \rho}{\rho} \quad (13.11)$$

The pressure change due to fluid motion can be estimated from the Bernoulli equation (see section 2.3.1, Eqn 2.6) as

$$\delta p \sim \frac{\rho}{2} V^2 \quad (13.12)$$

Substituting this value in Eqn 13.11, it follows

$$\frac{\delta \rho}{\rho} \sim \frac{1}{2} \frac{\rho}{p} V^2 \quad (13.13)$$

p and ρ denote here some value of pressure and density in the undisturbed region of flow, and may be considered as a set of constant reference values.

In physics textbooks it is shown that the speed of sound in a perfect gas is given by

$$a^2 = \frac{p}{\rho} \quad (13.14)$$

From Eqn 13.13 it follows

$$\frac{\delta\rho}{\rho} \sim \frac{1}{2} \frac{V^2}{a^2} = \frac{1}{2} Ma^2 \quad (13.15)$$

The abbreviation Ma for the ratio of flow velocity to the velocity of sound is called the Mach number. From Eqn 13.15 one can state that the effects of compressibility are negligible if the ensuing density change

$$\frac{\delta\rho}{\rho} \ll 1 \quad (13.16)$$

In other words, compressibility effects can be neglected if the Mach number of the flow remains small compared to unity. At normal temperature, the speed of sound in air is about 1332 km/h. Assuming the maximum speed for a utility road vehicle of 250 km/h, the resulting Mach number for the flow field is 0.19. From Eqn 13.15 the change in density amounts to about 2 per cent. In aeronautical practice, compressibility effects are usually ignored for flows with a Mach number below 0.3.

13.6 Two approximations for the fluid air

Some of the difficulties encountered when describing the vehicle flow field analytically have been indicated in the preceding sections. To render the problems of aerodynamics tractable, the physical properties of air have to be approximated. The approximations relevant to vehicle aerodynamics lead basically to two types of fluid namely, a perfect fluid and a viscous, incompressible fluid.

The perfect fluid is a homogeneous, inviscid and incompressible medium. From Eqns 13.9 and 13.15 it follows that, for an inviscid incompressible flow, the Reynolds number is infinite and the Mach number equals zero. Independence of such flows from Reynolds number means that, with this approximation, the scale effects cannot be considered in the analysis. Such flows are also termed 'potential' flows and are a good simulation for flow regions outside the boundary layer and wake.

Assuming the fluid to be a homogeneous, viscous and incompressible medium is an almost complete description of air for problems of vehicle aerodynamics. The Reynolds number is then finite and Mach number is zero. Viscous laminar flow is amenable to accurate numerical analysis. Treatment of viscous turbulent flow is difficult and tractable mostly with the help of semi-empirical formulations.

13.7 Inviscid flow methods

13.7.1 Governing equations

The equations of motion for an inviscid, incompressible perfect fluid can be derived from the Navier-Stokes equations. For an unbounded, homogeneous, viscous and incompressible fluid, the Navier-Stokes equations express the balance between inertial force, pressure force and

viscous force, see e.g. refs 13.1 and 13.2. For a perfect fluid, as mentioned in the preceding section, the viscous force is absent and the set of equations of motion for a three-dimensional flow in cartesian coordinates is

$$\rho \left(\frac{\partial u}{\partial t} + u \frac{\partial u}{\partial x} + v \frac{\partial u}{\partial y} + w \frac{\partial u}{\partial z} \right) = - \frac{\partial p}{\partial x} \quad (13.17a)$$

$$\rho \left(\frac{\partial v}{\partial t} + u \frac{\partial v}{\partial x} + v \frac{\partial v}{\partial y} + w \frac{\partial v}{\partial z} \right) = - \frac{\partial p}{\partial y} \quad (13.17b)$$

$$\rho \left(\frac{\partial w}{\partial t} + u \frac{\partial w}{\partial x} + v \frac{\partial w}{\partial y} + w \frac{\partial w}{\partial z} \right) = - \frac{\partial p}{\partial z} \quad (13.17c)$$

The terms on the left-hand side express the inertial force and on the right-hand side the pressure force acting on a fluid element. In the above equations u, v, w are components of the velocity vector \vec{V} in the directions x, y and z , ρ the density and p the pressure.

For an incompressible fluid, from the law of conservation of mass, the equation of continuity follows as

$$\frac{\partial u}{\partial x} + \frac{\partial v}{\partial y} + \frac{\partial w}{\partial z} = 0 \quad (13.18)$$

The four unknowns u, v, w and p may be determined from the set of Eqns 13.17a,b,c and 13.18. Equations 13.17a,b,c are known in the literature as Euler's equations.

13.7.2 Irrotational flow field as a solution of the Euler equations

In spite of their seeming complexity the Euler equations can be integrated for an irrotational flow. A flow is said to be irrotational if the components of the vorticity vector $\vec{\omega}$ are equal to zero everywhere in the flow field. With

$$\vec{\omega} = i\omega_x + j\omega_y + k\omega_z \quad (13.19)$$

and

$$\begin{aligned} \omega_x &= \frac{1}{2} \left(\frac{\partial w}{\partial y} - \frac{\partial v}{\partial z} \right) \\ \omega_y &= \frac{1}{2} \left(\frac{\partial u}{\partial z} - \frac{\partial w}{\partial x} \right) \\ \omega_z &= \frac{1}{2} \left(\frac{\partial v}{\partial x} - \frac{\partial u}{\partial y} \right) \end{aligned} \quad (13.20)$$

the irrotationality of flow implies that

$$\omega_x = \omega_y = \omega_z = 0 \quad (13.21)$$

The condition of irrotationality can be derived directly from the Euler equations (13.17) with the help of the continuity equation (13.18), see e.g. refs 13.1 and 13.2. To restate the problem of integration of the Euler equations: if a flow field satisfies the condition of irrotationality, Eqn

13.20, and the condition of continuity, Eqn 13.18, it represents a solution of the Euler equations.

13.7.3 Consequences of irrotational motion

A flow whose velocity field is irrotational can be expressed as the gradient (denoted by grad) of a scalar potential function $\Phi(x,y,z)$, see e.g. refs. 13.1, 13.2 and 13.3. The velocity potential Φ is defined as continuous and differentiable throughout the entire flow regime. It is

$$\vec{V}(x,y,z) = \text{grad } \Phi = i \frac{\partial \Phi}{\partial x} + j \frac{\partial \Phi}{\partial y} + k \frac{\partial \Phi}{\partial z} \quad (13.22)$$

With $\vec{V} = iu + jv + kw$, the components of the velocity are given by

$$u = \frac{\partial \Phi}{\partial x}; \quad v = \frac{\partial \Phi}{\partial y}; \quad w = \frac{\partial \Phi}{\partial z} \quad (13.23)$$

For the x -component of vorticity vector ω_x , it follows from Eqns 13.20 and 13.23

$$\omega_x = \frac{1}{2} \left(\frac{\partial^2 \Phi}{\partial y \partial z} - \frac{\partial^2 \Phi}{\partial y \partial z} \right) = 0$$

Similarly

$$\omega_y = \omega_z = 0$$

Thus the condition of irrotationality is fulfilled by the potential function Φ . Substituting Eqn 13.23 in the continuity equation (13.18), one obtains

$$\frac{\partial^2 \Phi}{\partial x^2} + \frac{\partial^2 \Phi}{\partial y^2} + \frac{\partial^2 \Phi}{\partial z^2} = 0 \quad (13.24)$$

Using the Laplace operator

$$\nabla^2 = \frac{\partial^2}{\partial x^2} + \frac{\partial^2}{\partial y^2} + \frac{\partial^2}{\partial z^2}$$

Eqn 13.24 can be expressed as

$$\nabla^2 \Phi = 0 \quad (13.25)$$

Eqn 13.25 is known in the literature as the Laplace or potential equation.

The introduction of the concept of a potential function considerably simplifies the problem of integration of the Euler equations. Instead of seeking a solution of the three non-linear partial differential equations 17a,b,c together with the equation of continuity, Eqn 13.18, it is sufficient to find a solution for the potential function Φ which fulfils Eqn 13.25. From a mathematical viewpoint, the solution of the linear Laplace equation (13.25) is much simpler than the non-linear set of Euler equations. Linearity of the Laplace equation allows the generation of a family of solutions from a set of known basic solutions using the principle of superposition. If

$$\begin{aligned}
&\Phi_1(x, y, z) \\
&\Phi_2(x, y, z) \\
&\vdots \\
&\Phi_n(x, y, z)
\end{aligned}$$

represent n basic solutions of the Laplace equation, then

$$\Phi(x, y, z) = a_1\Phi_1 + a_2\Phi_2 + \dots + a_n\Phi_n \quad (13.26)$$

also represents a solution of the Laplace equation.^{13.2} Through proper choice of the constants a_1, a_2, \dots, a_n , particular solutions can be 'constructed'.

Since each of the solutions $\Phi_1, \Phi_2, \dots, \Phi_n$ is linear, the velocity components and therefore the velocity vectors are also additive. This means that, with (see Eqn 13.23),

$$\begin{aligned}
u &= \frac{\partial \Phi}{\partial x} ; \quad v = \frac{\partial \Phi}{\partial y} ; \quad w = \frac{\partial \Phi}{\partial z} \\
u_1 &= \frac{\partial \Phi_1}{\partial x} ; \quad v_1 = \frac{\partial \Phi_1}{\partial y} ; \quad w_1 = \frac{\partial \Phi_1}{\partial z} \\
u_2 &= \frac{\partial \Phi_2}{\partial x} ; \quad v_2 = \frac{\partial \Phi_2}{\partial y} ; \quad w_2 = \frac{\partial \Phi_2}{\partial z} \\
&\vdots \\
u_n &= \frac{\partial \Phi_n}{\partial x} ; \quad v_n = \frac{\partial \Phi_n}{\partial y} ; \quad w_n = \frac{\partial \Phi_n}{\partial z}
\end{aligned}$$

the resultant velocity field $\vec{V}(x, y, z)$ can be expressed as

$$\vec{V}(x, y, z) = \left. \begin{aligned} &i(a_1u_1 + a_2u_2 + \dots + a_nu_n) + \\ &j(a_1v_1 + a_2v_2 + \dots + a_nv_n) + \\ &k(a_1w_1 + a_2w_2 + \dots + a_nw_n) \end{aligned} \right\} \quad (13.26)$$

From the velocity field, the pressure field $p(x, y, z)$ can be evaluated using the Bernoulli equation (Eqn 2.7)

$$p + \frac{\rho}{2} V^2 = \text{const.} \quad (13.27)$$

It is important to note that the pressures p_1, p_2, \dots, p_n of the basic flows cannot be superimposed because of the quadratic relation between pressure and velocity (Eqn 13.27).

13.7.4 Stream function

A useful concept in the treatment of irrotational flows is that of a stream function. As seen in section 13.7.3, the potential function Φ fulfils the condition of irrotationality. The equation of continuity (13.24), is then used to evaluate the potential function. Alternatively, it is possible to

define a function ψ , which fulfils the equation of continuity. The condition of irrotationality can then be used to determine the function ψ .

The function ψ is termed the stream function. A unique definition of the stream function is possible for two-dimensional flow. Such a function can also be found in three dimensions for the case of axially symmetric flows, see for example refs 13.3 and 13.4.

For the sake of simplicity, we consider below a two-dimensional flow. The stream function $\psi(x,y)$ can be expressed in terms of the velocity components u and v as

$$u = \frac{\partial \psi}{\partial y}, \quad v = -\frac{\partial \psi}{\partial x} \quad (13.28)$$

Substituting this in the continuity equation for two-dimensional incompressible flow

$$\frac{\partial u}{\partial x} + \frac{\partial v}{\partial y} = 0 \quad (13.29)$$

it is seen that Eqn 13.9 is fulfilled.

For a two-dimensional flow, with only velocity components u and v present, the condition of irrotationality (Eqn 13.20) reduces to

$$\omega_z = 0$$

$$\text{or} \quad \frac{\partial v}{\partial x} - \frac{\partial u}{\partial y} = 0 \quad (13.30)$$

Equation 13.30 can be used to determine the stream function $\psi(x,y)$. Substituting for u and v from Eqn 13.28

$$\frac{\partial^2 \psi}{\partial x^2} + \frac{\partial^2 \psi}{\partial y^2} = 0 \quad (13.31)$$

The stream function can be utilized to map the streamlines in a flow field. A streamline is a curve whose tangent at every point in the flow coincides with the direction of the velocity vector.

From Eqn 13.22 a two-dimensional potential flow is given by the velocity field

$$\vec{V}(x,y) = \text{grad} [\Phi(x,y)] = i \frac{\partial \Phi}{\partial x} + j \frac{\partial \Phi}{\partial y} \quad (13.32)$$

and

$$\text{grad} \Phi = iu + jv \quad (13.33)$$

The gradient of the stream function is given by Eqn 13.28

$$\text{grad} \psi = i \frac{\partial \psi}{\partial x} + j \frac{\partial \psi}{\partial y} = -iv + ju \quad (13.34)$$

A comparison of Eqns 13.33 and 13.34 shows that the vectors $\text{grad} \Phi$ and $\text{grad} \psi$ are perpendicular to one another (Fig. 13.2). It can be shown that the vectors $\text{grad} \Phi$ and $\text{grad} \psi$ point in the direction normal to the curves $\Phi = \text{const.}$ and $\psi = \text{const.}$ respectively.^{13.3} The vector $\text{grad} \Phi$, which

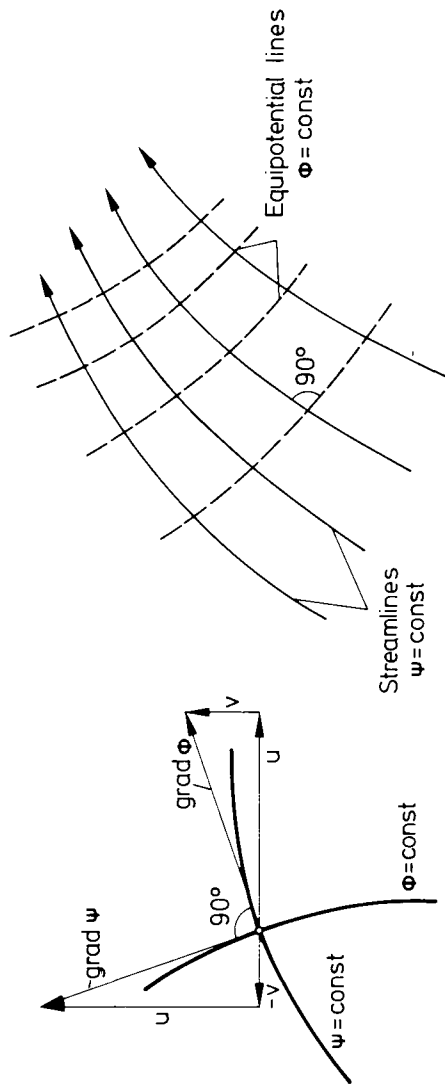


Figure 13.2 Streamlines and equipotential lines are orthogonal

represents the velocity vector, is thus tangential everywhere to the curve $\psi = \text{const.}$ Therefore the curves $\psi = \text{const.}$ represent the streamlines of the flow. From the above it also follows that streamlines ($\psi = \text{const.}$) and equipotentials ($\Phi = \text{const.}$) are orthogonal (Fig. 13.2).

13.7.5 Some basic potential flows

In this section some well-known basic potential flows are treated briefly. Using the principle of superposition, complicated potential flows of practical interest can be 'constructed' with these basic solutions. Use is made of this technique in the vortex lattice and panel methods, to be treated later in this chapter.

13.7.5.1 Uniform flow

A uniform flow with the velocity vector $\vec{V} = iu + jv + kw$, constant everywhere in a flow region can be represented by the potential function

$$\Phi(x, y, z) = ux + vy + wz \quad (13.35)$$

with

$$u = \frac{\partial \Phi}{\partial x}, \quad v = \frac{\partial \Phi}{\partial y} \text{ and } w = \frac{\partial \Phi}{\partial z}$$

Since u , v and w are also constant in the flow field, the potential function defined by Eqn 13.35 fulfils the continuity equation (13.24). The streamlines of the uniform flow are straight lines oriented in space such that their intercepts with a cartesian axis system are given by

$$dx : dy : dz = u : v : w \quad (13.36)$$

13.7.5.2 Point source or sink flow

If the streamlines of a flow emanate radially from a point, the flow field created is said to be a source flow. The potential function of a three-dimensional source flow is given by

$$\Phi(x, y, z) = -\frac{Q}{4\pi} \frac{1}{r} \quad (13.36)$$

with $r = \sqrt{(x^2 + y^2 + z^2)}$. The velocity components of the source flow in cartesian coordinates are obtained from Eqn 13.36 as

$$\begin{aligned} u &= \frac{Q}{4\pi} \frac{x}{r^3} \\ v &= \frac{Q}{4\pi} \frac{y}{r^3} \\ w &= \frac{Q}{4\pi} \frac{z}{r^3} \end{aligned} \quad (13.37)$$

The equipotential surfaces $\Phi = \text{const.}$ are spheres of radii r with the origin at $x = y = z = 0$. The resultant velocity \vec{V} of the flow is directed radially outwards, i.e. normal to the surface of the spherical equipotential surfaces. It is

$$V(r) = \sqrt{(u^2 + v^2 + w^2)} = \frac{Q}{4\pi} \frac{1}{r^2} \quad (13.38)$$

The outflowing volume of fluid through a closed spherical surface of radius r is given by

$$\text{Volume} = V \cdot 4\pi r^2 = \frac{Q}{4\pi} \frac{1}{r^2} \cdot 4\pi r^2 = Q \quad (13.39)$$

Since the chosen value of r is arbitrary, it follows from Eqn 13.39, that the outflow of fluid through any closed spherical surface with its origin at the origin of the axes is constant and equals Q . Q is termed the strength of the source, or simply source strength.

For positive values of Q , we see from Eqn 13.38 that fluid is being continuously 'created' at the point $r = 0$. In the case of Q being negative, the velocity $V(r)$ is directed radially inwards and the fluid continuously 'disappears' at the point $r = 0$. A radially inwards-directed flow, analogous to the source, is called a sink flow. The corresponding potential function and the velocity components can be readily obtained from Eqns 13.36, 13.37 and 13.38 by putting $Q = -Q$.

It is important to note that the velocity $V(r)$ becomes infinite at the point $r = 0$ (Eqn 13.38). The origin, $r = 0$, represents a singular point, also characterized by 'creation' and 'disappearance' of fluid there. As this is not possible in nature, the source or sink flow described above has relevance to reality only when the immediate vicinity of the singular point $r = 0$ is omitted from consideration.

13.7.5.3 Plane source or sink flow

In a two-dimensional (plane) flow with only the velocity components u and v present, the potential function for a source or sink flow is

$$\Phi(x,y) = \frac{Q}{2\pi} \ln r \quad (13.40)$$

with

$$r = \sqrt{(x^2 + y^2)}$$

Source flow is represented by positive and sink flow by negative values of the strength Q .

The equipotential lines for a plane source or sink are concentric circles about the origin of the xy -axes (Fig. 13.3). Radially outward or inward directed straight rays from the origin represent the streamlines for a plane source or sink. The velocity components in cartesian coordinates are obtained from Eqn 13.40 as

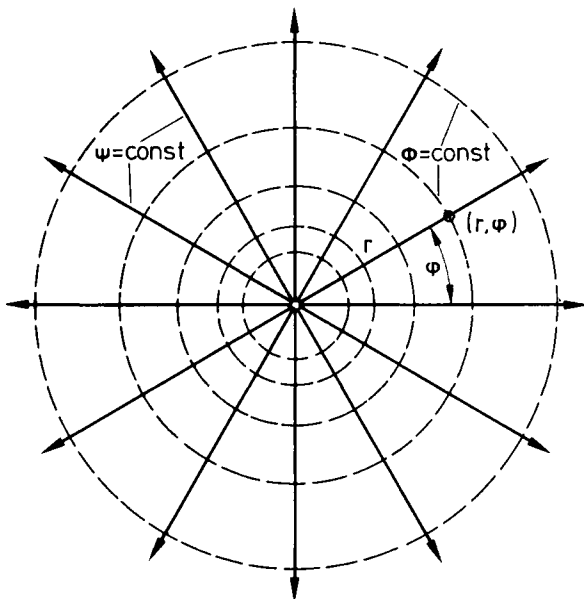


Figure 13.3 Streamlines and equipotential lines for a point source flow

$$u = \frac{Q}{2\pi} \frac{x}{r^2}$$

$$v = \frac{Q}{2\pi} \frac{y}{r^2}$$
(13.41)

and the resultant radially directed velocity

$$V(r) = \sqrt{(u^2 + v^2)} = \frac{Q}{2\pi} \frac{1}{r}$$
(13.42)

The stream function for the plane source or sink flow is

$$\psi(x, y) = \frac{Q}{2\pi} \arctan^{-1} \left(\frac{y}{x} \right) = \frac{Q}{2\pi} \varphi$$
(13.43)

with φ denoting the polar angle (Fig. 13.3).

As noted earlier in section 13.7.5.2, the origin $r = 0$ represents a singular point. Solutions of the Laplace equation (13.25) which contain such singular points are called singular solutions.

13.7.5.4 Point doublet and plane doublet

Another interesting singular solution of the Laplace equation (13.25) is obtained when a source of strength Q , and a sink of equal strength, situated at a distance l apart, are brought together by letting l go to zero. The resulting flow has the potential^{13.1}

$$\Phi(x, y, z) = M \frac{x}{r^3}$$
(13.44)

$$\text{with } r = \sqrt{(x^2 + y^2 + z^2)} \quad (13.45)$$

$$\text{and } M = \frac{Ql}{4\pi}$$

The product $M = Ql/4\pi$ is referred to as the doublet strength and also as the moment of the doublet.

Velocity components in the x , y and z -directions are obtained from Eqn 13.44 as

$$\begin{aligned} u &= M \frac{r^2 - 3x^2}{r^5} \\ v &= -M \frac{xy}{r^5} \\ w &= -M \frac{xz}{r^5} \end{aligned} \quad (13.46)$$

In a spherical coordinate system defined by R , θ and φ , the streamlines are given in a plane $\varphi = \text{const.}$ by (see e.g. ref. 13.3)

$$\frac{\sin^2 \theta}{R} = \text{constant} \quad (13.47)$$

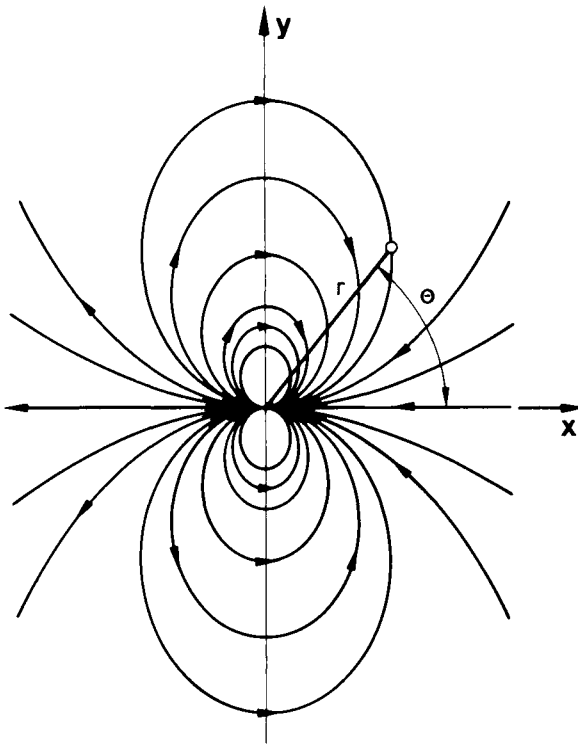


Figure 13.4 Streamlines for a point doublet

Figure 13.4 shows the streamlines for a point doublet. The streamlines are obtained by choosing different values for the constant in Eqn 13.47.

Similar considerations lead to the derivation of potential and stream functions for a plane doublet.^{13.1}

In terms of cartesian coordinates, the potential function is

$$\Phi(x,y) = M_p \frac{x}{r^2} \quad (13.48)$$

and the stream function

$$\psi(x,y) = -M_p \frac{y}{r^2} \quad (13.49)$$

As before, $M_p = Ql/2\pi$, is termed as the doublet strength or moment of the plane doublet.

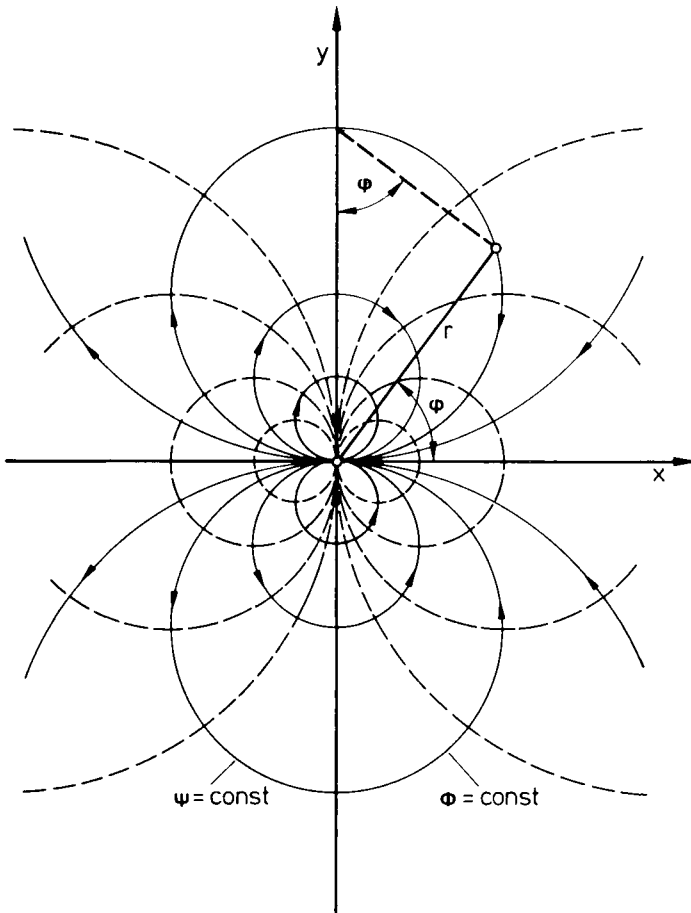


Figure 13.5 Streamlines and equipotential lines for a plane doublet

The components of velocity u and v follow from Eqn 13.48, as

$$u = -M_p \frac{y^2 - x^2}{r^4} \quad (13.50)$$

$$v = -M_p \frac{2xy}{r^4}$$

Equipotential lines and streamlines for a plane doublet can be readily derived from Eqns 13.48 and 13.49 and are shown in Fig. 13.5. Streamlines and equipotential lines are represented by a family of circles tangent to the x -axis or the y -axis respectively.

13.7.5.5 Point vortex and vortex filament

A potential flow of great importance in aerodynamics is that of a vortex. The potential function

$$\Phi(x,y) = \frac{\Gamma}{2\pi} \arctan \left(\frac{y}{x} \right) = \frac{\Gamma}{2\pi} \varphi \quad (13.51)$$

with the corresponding stream function

$$\Psi(x,y) = -\frac{\Gamma}{2\pi} \ln (x^2 + y^2) = -\frac{\Gamma}{2\pi} \ln r \quad (13.52)$$

is that of a point vortex of 'strength' Γ situated at the origin $x = y = 0$ (Fig. 13.6). The equipotential and streamlines of a vortex flow are straight

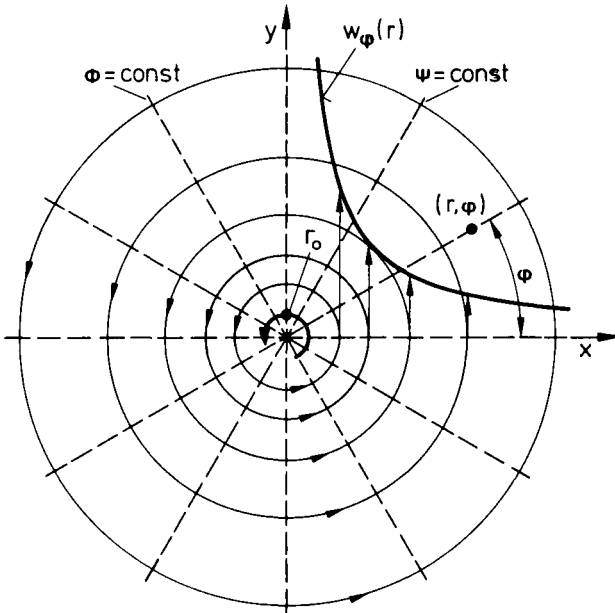


Figure 13.6 Streamlines, equipotential lines and circumferential velocity distribution of a point vortex

outward rays emanating from the origin and concentric circles about it, respectively. The velocity component of the flow along an outward ray

$$w_r = \frac{\partial \Phi}{\partial r} = 0 \quad (13.53)$$

i.e. the radial component of the velocity for a vortex flow is equal to zero. (It can be shown that the velocity component of a potential flow in a direction n is given by the derivative $\partial \Phi / \partial n$; see e.g. ref. 13.3.) Components of the velocity in x - and y -directions are given by

$$\begin{aligned} u &= -\frac{\Gamma}{2\pi} \frac{y}{r^2} \\ v &= \frac{\Gamma}{2\pi} \frac{x}{r^2} \end{aligned} \quad (13.54)$$

The velocity vector \vec{V} is

$$\vec{V}(x,y) = iu + jv$$

and

$$V = \frac{1}{r} \frac{\Gamma}{2\pi} \quad (13.55)$$

As the streamlines are concentric circles and no radial component of velocity is present, the resultant velocity V from Eqn 13.55 is the circumferential velocity in the circulatory vortex flow.

It is customary to speak of the flow defined by Eqns 13.51 and 13.52 as that of a point vortex. The two-dimensional velocity field described by Eqn 13.54 is that of a vortex flow in the xy plane with the point vortex at the origin $x = y = 0$. Two-dimensional flow implies that the flow pattern is identical in all planes parallel to the xy plane. The line connecting the origins of the vortex flow in these parallel planes is a straight vortex filament.

In three-dimensional flow, a line coinciding with the axis of rotation of successive fluid elements is termed a vortex filament. This flow too possesses a singularity at the point $r = 0$ (see Eqn 13.55) where the velocity becomes infinite and thus is physically impossible. However, vortex flows occur in a viscous fluid, outside the central core of the flow field, which conform closely with that described by Eqns 13.51 and 13.52.

From Eqn 13.55 it can be seen that

$$2\pi rV = \Gamma = \text{constant} \quad (13.56)$$

irrespective of the chosen radius r . The product of circumference ($= 2\pi r$) and velocity V , is called the strength of the vortex filament and denoted by Γ .

13.7.6 Some concepts common to vortex-lattice and panel methods

Before dealing with the vortex-lattice and panel methods in more detail, some common features of these inviscid flow approaches as applied to

computation of vehicle flow fields are presented in this section. The analytical concept for the simulation of a potential flow around an arbitrarily shaped body is to consider the flow to be formed by the superposition of two flow fields: A uniform 'onset' flow field of constant velocity \vec{V}_∞ and a 'perturbation' flow field with velocity $\vec{V}_p(x,y,z)$.

The uniform onset flow is defined as the one which would exist in the absence of the body. Perturbation flow is so structured that at every point in the flow field the actual velocity vector $\vec{V}(x,y,z)$ is given by the resultant of both flow fields:

$$\vec{V}(x,y,z) = \vec{V}_\infty + \vec{V}_p(x,y,z) \quad (13.57)$$

In the vehicle flow problem considered here, the onset flow is known. For a vehicle moving with a constant speed this is, for example, a field with a constant velocity \vec{V}_∞ equal to the vehicle velocity.

Given the geometry of the vehicle and the onset flow, the problem is therefore to find the appropriate perturbation velocity field $\vec{V}_p(x,y,z)$. Relevance of the solution to the specific nature of a particular case is obtained by imposing boundary conditions on the solution. From physical considerations, it is plausible that an inviscid fluid glides past the body surface without being decelerated. The resulting flow appears tangentially attached everywhere on the body surface. In other words, on the body surface, the normal component of the resultant flow velocity \vec{V} can be set equal to zero.

A further boundary condition also following from physical observation concerns the perturbation flow. The perturbation of the onset flow is strongest on the body surface. This effect diminishes as the distance from the body surface increases. If Φ , Φ_0 and Φ_p denote the potentials of the resultant flow, onset flow and the perturbation flow respectively, the two boundary conditions stated above can be expressed as

$$\frac{\partial \Phi}{\partial n} = \frac{\partial \Phi_0}{\partial n} + \frac{\partial \Phi_p}{\partial n} = 0 \quad (13.58)$$

$$\Phi_p \rightarrow 0 \quad \text{with} \quad r \rightarrow \infty$$

In Eqn 13.58 n is the direction normal to body surface and r is the distance away from a point on the body surface.

The flow around a bluff-based ground vehicle is characterized in the real flow by the presence of a wake which emanates from the rear part of the body surface. It is also known that ground vehicles can experience a sizeable amount of lift.

The wake and the trailing vorticity shed by a lifting body are simulated by an artifact in potential flow methods. This consists of an infinitely thin tubular surface which extends downstream in direction of the onset flow, starting from a postulated flow separation line round the rear end of the body. Shed vorticity is assumed to be concentrated in this infinitely thin surface which now represents the wake in the analytical model.

In the real flow, the wake 'surface' is aligned in the direction of the local velocity; i.e. the wake 'surface', in contrast to the body surface, cannot carry a load; instead it deforms until its surface is load-free. For a given

body and flow conditions, the geometry of the wake boundary surface is not known in advance. This non-linear problem is often linearized in practice by the assumption of a certain geometrical shape for the wake surface.

In the case of a road vehicle, the ground plane simulation is effected by introducing an image of the road vehicle symmetrically below the notional position of the ground plane. The inviscid flow produced by the vehicle and its image is symmetrical to the ground plane. The plane of symmetry is a stream surface and represents the inviscid flow over the plane ground surface.

13.7.7 The vortex-lattice method

The fundamental ideas underlying the vortex-lattice approach are derived from the concept of a 'lifting surface', which is well known in aerodynamics.^{13.2,13.5}

Considering the flow around a road vehicle, its 'wetted' surface is approximated by flat area elements, each of which is simulated in the flow model by a discrete 'horseshoe' vortex. A horseshoe vortex consists of a 'bound' leg filament and two 'trailing' leg filaments. The bound leg of the horseshoe vortex is placed on the upstream element edge, and its trailing legs are positioned along its sides as illustrated in Fig. 13.7. The trailing

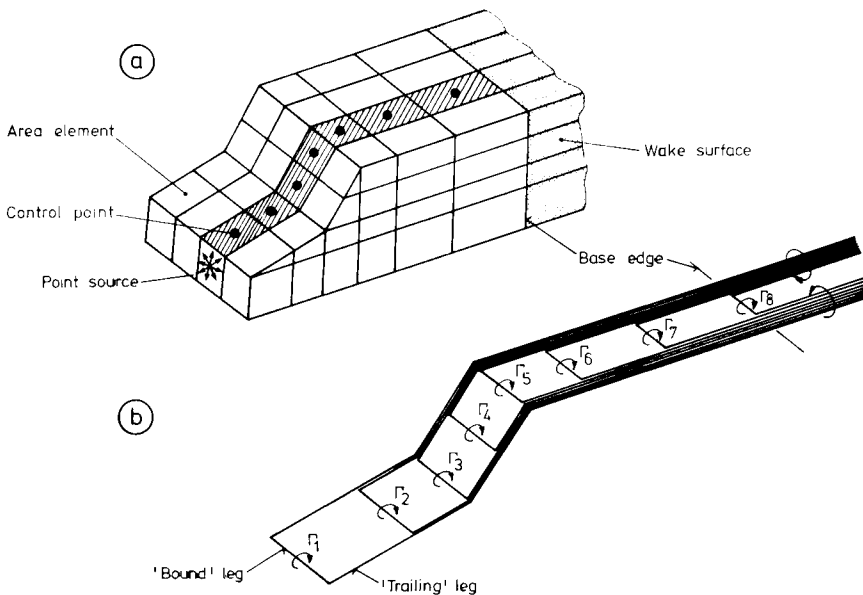


Figure 13.7 (a) Surface discretization for vortex lattice layout (schematic), and (b) arrangement of horseshoe vortices on a surface strip

legs are positioned in the plane of their originating element, and are deflected so that they lie in the plane of each surface element downstream of the originating element. From the last surface element contacted, i.e. at the edge of the flat vehicle base, the trailing legs extend downstream. The

trailing legs of the individual horseshoe vortices are placed coincident with the element side edges and are consequently contiguous with adjacent horseshoe vortices. The strength of a trailing leg is thus the vector sum of adjacent horseshoe vortex strengths. Figure 13.7b shows the vortex-lattice arrangement for a surface strip (shaded) of Fig. 13.7a.

The boundary condition, expressing flow tangency to body surface, is satisfied at a number of 'control points' which, for example, can be the centroids of area elements.

The geometry of the wake surface that emanates from the vehicle base is not known. To render the problem linear, its shape has to be assumed. To impose the flow tangency condition on this wake surface implies that it should represent a stream surface in the computed flow. A stream surface of the assumed wake shape may however not exist in the computed flow. The error involved depends on the accuracy with which wake geometry can be determined. Wake simulation thus remains inadequate in the linear theoretical model under consideration here.

Stafford,^{13.6,13.7} in applying the vortex-lattice method to compute the flow around a motor car, excludes the base area, which is covered by the wake, from the surface simulation. Through the open rear end an outflow is generated by placing a point source within the body. The strength of this source is given by the product of the open base area and the onset flow velocity. The position of the source within the body is adjusted to satisfy a flow tangency condition on an area element of body surface. This tubular wake of constant cross-section extends downstream to infinity. Accordingly, the trailing legs of vortex filaments coming off the vehicle base also extend to infinity. The surface of the wake is not discretized and no boundary conditions are imposed on it.

As noted earlier, the resulting flow field is obtained through superposition of a uniform onset flow and the perturbation flow created by the horseshoe vortices placed on the body surface. The total velocity at a point is the vector sum of the onset flow velocity and induced velocity contributions of all vortex filaments on the body and the trailing filaments. The induced velocity through a vortex filament at a point is given by the Biot-Savart law (see e.g. refs 13.2 and 13.3).

In Fig. 13.7 $\Gamma_1, \Gamma_2 \dots \Gamma_n$ denote the vortex strengths of horseshoe vortices placed on n area elements of the surface. Let a_{ij} represent the velocity induced by a horseshoe vortex of unit strength, placed on the j th element, at the control point of the area element i . If A_{ij} is the component of this induced velocity in a direction normal to the surface of the area element i , then

$$\sum_{j=1}^n A_{ij} \Gamma_j \quad (13.59)$$

is the total normal velocity induced by all vortex filaments at control point of area element i . For a body in ground proximity, the terms a_{ij} and A_{ij} include the influence of vortex-lattice body 'image' arranged below the ground; see section 13.7.6. To satisfy the boundary condition of flow tangency, i.e. no flow across the surface of the element i , this velocity

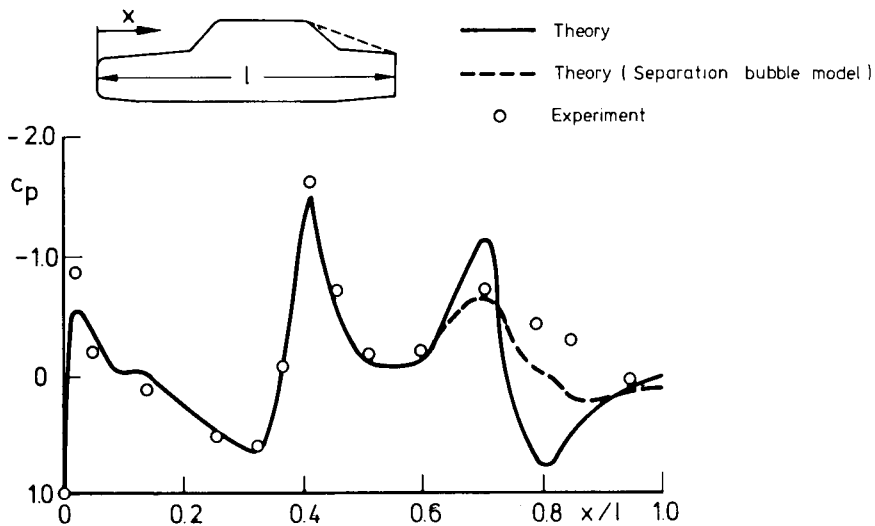


Figure 13.8 Pressure coefficient distribution along centreline of saloon model (top surface), after ref. 13.6

the pressure distribution along the centre line of the upper surface. In general the agreement with experimental results is satisfactory in spite of the coarse surface discretization. Discrepancies at grille/hood and windscreen/roof junctions are probably due to insufficient surface element density. The main deviation of the theoretical results from experiment is however visible at the roof rear edge, where the flow separates in the wind tunnel experiment. The inviscid theoretical model obviously cannot simulate this phenomenon. By changing the model contour to follow the dotted line from roof rear edge to the boot edge, an improved pressure prediction is obtained. The dotted line in Fig. 13.8 can be assumed to represent crudely the 'separation bubble' contour. A separation bubble exists in the real flow between the rear window and boot lid region. It is interesting to note that the pressure computed at the assumed 'edge' of this separation bubble gives a better estimate of the pressure values measured on the model surface.

In a further study, Stafford^{13.7} demonstrated that some improvements in pressure prediction are possible through a more adequate wake modelling.

13.7.8 The panel method

Some of the difficulties involved in 'constructing' a perturbation flow model for the road vehicle problem were evident in the preceding section. In textbooks of fluid mechanics it is shown that to simulate the flow about a lift-generating body of finite thickness both sources/sinks and doublet/vortex types of singularities must be present in the theoretical model, (see e.g. refs 13.2, 13.3, 13.5). To circumvent this difficulty of the vortex-lattice approach to vehicle flow problem, Stafford^{13.6} employed a point source, placed within the body, which was otherwise represented only by a vortex lattice.

The panel method, discussed in this section, generates the perturbation flow by a source/sink singularity sheet placed on the surface of the body (Fig. 13.9a). For lifting bodies, doublet or vortex sheets are introduced to provide circulation. The strength of the singularity sheet varies over the surface in a manner such that at every point on the solid body (and wake) surface the normal velocity generated by the singularity sheet(s) just balances the component of the onset flow velocity. It is not necessary that the singularity sheets coincide with the surface on which the boundary conditions themselves are applied.

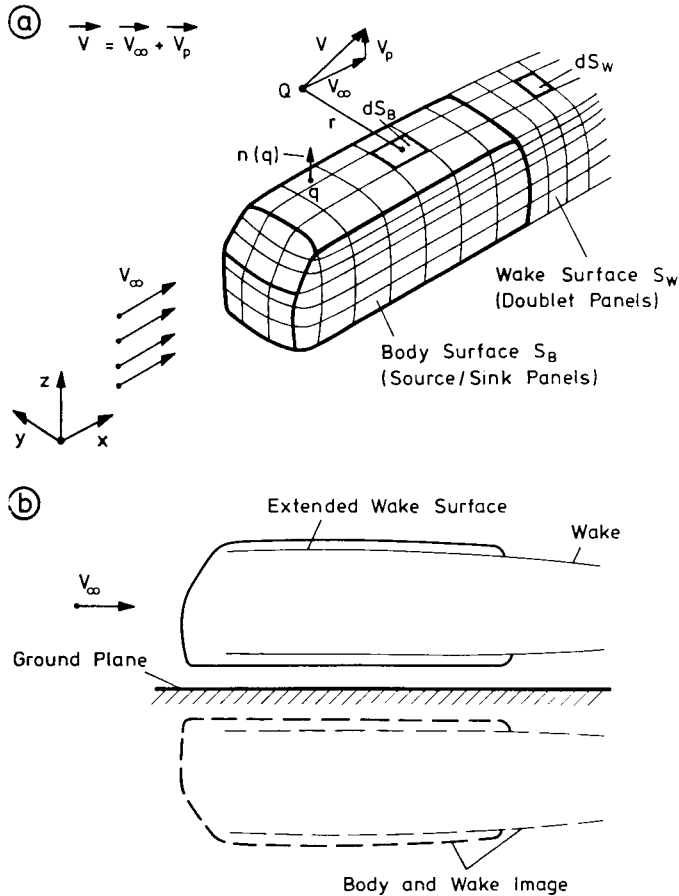


Figure 13.9 Numerical simulation of a vehicle model by the panel method

The essential features of the panel method formulated to compute a vehicle flow field are illustrated in Fig. 13.9 (from ref. 13.8). Let $\sigma(S_B)$ be the local strength of the source sheet placed on the body surface S_B and $\mu(S_W)$ the local strength of the doublet sheet representing the assumed wake surface S_W . If Q is a point in the flow field at a distance r from a characteristic point ('control point') of the body and wake surface, then the potential at Q due to source/sink sheet can be expressed as

$$\varphi_s(Q) = - \frac{1}{4\pi} \iint_{S_B} \frac{\sigma(S_B)}{r} dS_B \quad (13.62)$$

and the potential due to a doublet sheet as

$$\varphi_D(Q) = \frac{1}{4\pi} \iint_{S_w} \mu(S_w) \frac{\partial}{\partial n} \left(\frac{1}{r} \right) dS_w \quad (13.63)$$

The integration in Eqns 13.62 and 13.63 is to be performed over the body and wake surface. The expression $\partial/\partial n$ in Eqn 13.63 is the derivative in the direction normal to the surface.

The total perturbation potential $\varphi(Q)$ at point Q is given by the sum of the potentials φ_s and φ_D :

$$\varphi(Q) = \varphi_s(Q) + \varphi_D(Q) \quad (13.64)$$

It is worth while noting that, with ground simulation through the image technique (see section 13.7.6), every body and wake point has a counterpart in its image below the ground. Each of the terms in Eqn 13.64 is thus to be interpreted as a sum of the contributions from a point and its image counterpart.

The resultant flow \vec{V}_∞ around the vehicle is obtained by superposing a uniform onset flow $\vec{V}_\infty(x,y,z)$ and the perturbation flow defined by $\sigma(S_B)$ and $\mu(S_w)$. In ref. 13.8, the flow tangency condition is applied on both body *and* wake surface. The wake surface geometry was evaluated by means of smoke visualization in a wind tunnel. This provided a better basis for assuming the wake surface to be a stream surface (see section 13.7.7). Considering a point q on the body surface, the flow tangency condition implies that the normal component of the perturbation velocity there just balances the normal component of onset velocity; i.e.

$$\text{grad} [\varphi(q)] \vec{n}(q) = -\vec{V}_\infty \vec{n}(q) \quad (13.65)$$

Substituting for $\varphi(q)$ from Eqns 13.64, 13.63 and 13.62, it follows that

$$\begin{aligned} \text{grad} \left[-\frac{1}{4\pi} \iint_{S_B} \frac{\sigma(S_B)}{r} dS_B + \frac{1}{4\pi} \iint_{S_w} \mu(S_w) \frac{\partial}{\partial n} \left(\frac{1}{r} \right) dS_w \right] \vec{n}(q) \\ = -\vec{V}_\infty \vec{n}(q) \end{aligned} \quad (13.66)$$

The source and doublet strength functions $\sigma(S_B)$ and $\mu(S_w)$ are unknown, so that Eqn 13.66 is non-linear. This equation links the unknowns σ and μ with the known body and wake surface geometry expressed through the surface normal vector \vec{n} . The onset velocity field $\vec{V}_\infty(x,y,z)$ is also known.

13.7.8.1 Numerical solution procedure

For the numerical solution, the continuous body and wake surface is replaced by flat quadrilateral or triangular area elements called panels (Fig. 13.9a). The source or doublet strength over the area of a panel is assumed constant. Consequences of this approach are: (1) through surface discretization, the surface integration in Eqn 13.66 is reduced to evaluation of a finite number of integrals, one for each panel, and (2) since σ and μ are

set constant over a panel surface, these can be taken out of the integral and the term becomes linear.

If m panels are used for the body and n panels for the wake surface discretization, then the integrals in Eqn 13.66 can be expressed as

$$\oint\oint_{S_B} \frac{\sigma(S_B)}{r} dS_B = \sum_{j=1}^m \sigma_j \oint\oint_{S_j} \frac{1}{r} dS_j \quad (13.67)$$

and

$$\oint\oint_{S_w} \mu(S_w) \frac{\partial}{\partial n} \frac{1}{r} dS_w = \sum_{j=1}^n \mu_j \oint\oint_{S_j} \frac{\partial}{\partial n} \frac{1}{r} dS_j \quad (13.68)$$

Introducing the abbreviations

$$X_j = \sigma_j / (4\pi V_\infty)$$

$$Y_j = \mu_j / (4\pi V_\infty)$$

$$A_{qj} = [-\text{grad} \oint\oint_{S_j} \frac{1}{r} dS_j] \vec{n}(q) \quad (13.69)$$

$$B_{qj} = \left[\text{grad} \oint\oint_{S_j} \frac{\partial}{\partial n} \left(\frac{1}{r} \right) dS_j \right] \vec{n}(q),$$

Eqn 13.66 reduces to:

$$\sum_{j=1}^m X_j A_{qj} + \sum_{j=1}^n Y_j B_{qj} = R_q \quad (13.70)$$

Equation 13.70 is a linear algebraic equation expressing the flow tangency condition at point q . X_j and Y_j express in dimensionless form the source and doublet strength of panel j . A_{qj} and B_{qj} can be interpreted as the normal component of the induced velocity at point q by a singularity distribution of unit strength placed on panel j . A_{qj} and B_{qj} are often termed the 'influence coefficients'. Repeated application of Eqn 13.70 to satisfy the flow tangency condition at m body and n wake surface control points leads to the linear system of $(m + n)$ equations:

$$\begin{bmatrix} A_{11}, A_{12} \dots A_{1m} & , B_{11}, B_{12} \dots B_{1n} \\ A_{21}, & \dots A_{2m} & , B_{21}, & \dots B_{2n} \\ \cdot & & \cdot & \\ \cdot & & \cdot & \\ \cdot & & \cdot & \\ A_{m1}, & \dots A_{mm} & , B_{m1}, & \dots B_{mn} \\ A_{(m+1)1} \dots A_{(m+1)m} & , B_{(m+1)1} & \dots B_{(m+1)n} \\ \cdot & & \cdot & \\ \cdot & & \cdot & \\ \cdot & & \cdot & \\ A_{(m+n)1} \dots A_{(m+n)m} & , B_{(m+n)1} & \dots B_{(m+n)n} \end{bmatrix} \begin{bmatrix} X_1 \\ X_2 \\ \cdot \\ \cdot \\ \cdot \\ X_m \\ Y_1 \\ \cdot \\ \cdot \\ \cdot \\ Y_n \end{bmatrix} = \begin{bmatrix} R_1 \\ R_2 \\ \cdot \\ \cdot \\ \cdot \\ R_m \\ R_{(m+1)} \\ \cdot \\ \cdot \\ \cdot \\ R_{(m+n)} \end{bmatrix} \quad (13.71)$$

Standard procedures, such as the Gauss-Seidel and Gauss-Jordan iteration schemes are employed to solve the equation system (13.71). With the

singularity strengths X_j and Y_j known, the perturbation potential at a surface point is evaluated from Eqns 13.67, 13.68 and 13.64.

Since the singularity strengths X_j and Y_j were determined by satisfying the flow tangency condition, the vector sum of perturbation velocity $\vec{V}_p(q) = \text{grad } \varphi(q)$ at a control point q and the onset velocity \vec{V}_∞ gives the tangential velocity at q . Using the Bernoulli equation, the pressure can now be evaluated. The force acting on a panel is then the product of this pressure (taken to be constant over the panel) and the panel area. The forces and moments acting on the body are given as the sum of those acting on the individual panels.

13.7.8.2 Examples of vehicle flow computations using the panel method

Ahmed and Hucho^{13.8} used the panel method to compute the inviscid flow around an idealized van. The theoretical simulation of both the body and the wake surface is simpler for this type of vehicle than a normal passenger car.

A quarter-scale wind tunnel model of the van was equipped with pressure taps and tested in the 7.5 by 5 metre wind tunnel of the Volkswagen AG at a model-length-based Reynolds number of 2.9×10^6 . All external surface details, such as headlights, bumpers, mirrors, window pockets etc. were removed and the surface smoothly faired. The wheel cavities were also filled and the underside was flat. Wheels were used to fix the model on a ground board. The numerical model in the panel method simulated the body and wake surface at the same height above the ground as the wind tunnel model. Not simulated were the wheels and the flat base surface covered by the wake. Cross-wind effects were investigated by yawing the uniform onset flow in the theoretical model. A total of 1652 panels was used to describe the body and the wake. The wake surface was modelled only up to one vehicle length behind the vehicle base. The results obtained showed that the errors caused by ignoring rest of the wake surface were insignificant.

Instead of simulating the ground by image technique as described in section 13.7.6, it is also possible to simulate the ground surface by 'panellizing' it and satisfying the flow tangency conditions on a road surface. A sufficiently large road area, ahead, behind and laterally, must be chosen to minimize the road area edge-interference effects. The advantage of this type of model is that the pressure distribution on a road surface can also be computed; see Fig. 12 of ref. 13.8.

Figure 13.10 illustrates the surface discretization used and the velocity distribution on the surface of the van obtained by computation for zero and non-zero cross-wind conditions. The length and orientation of the line segments corresponds to the magnitude and orientation of the velocity vectors. A stagnation region at the blunt front end, and high velocity at regions where front, side and upper surface blend together are visible. With cross-wind present, the stagnation region is shifted windwards, causing high velocity on windward-facing roof and side flank edges. Flow over the roof aligns itself mainly with the onset flow.

An impression of the accuracy of the numerical prediction is conveyed by the results shown in Fig. 13.11. As the numerical model is applicable

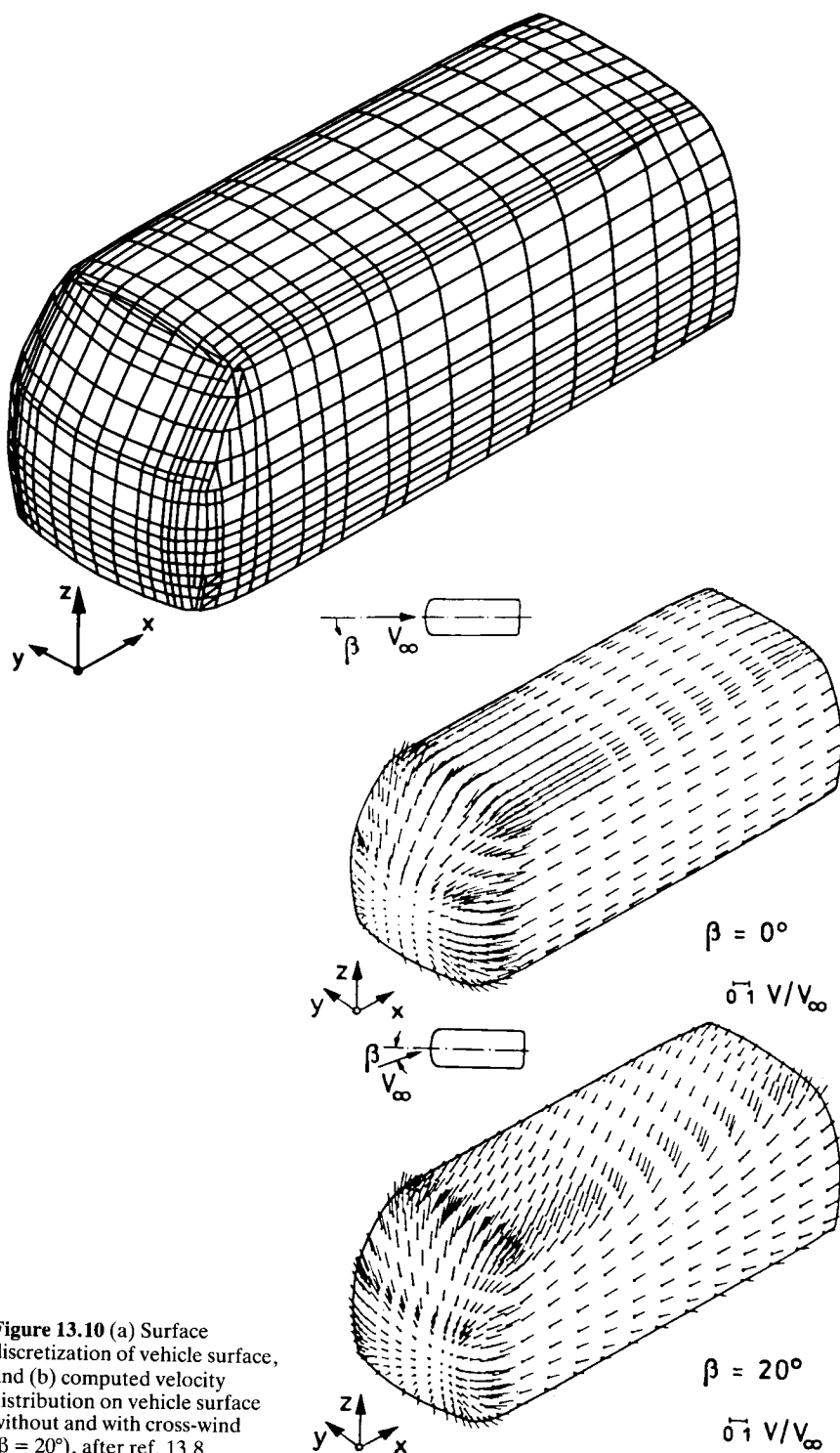


Figure 13.10 (a) Surface discretization of vehicle surface, and (b) computed velocity distribution on vehicle surface without and with cross-wind ($\beta = 20^\circ$), after ref. 13.8

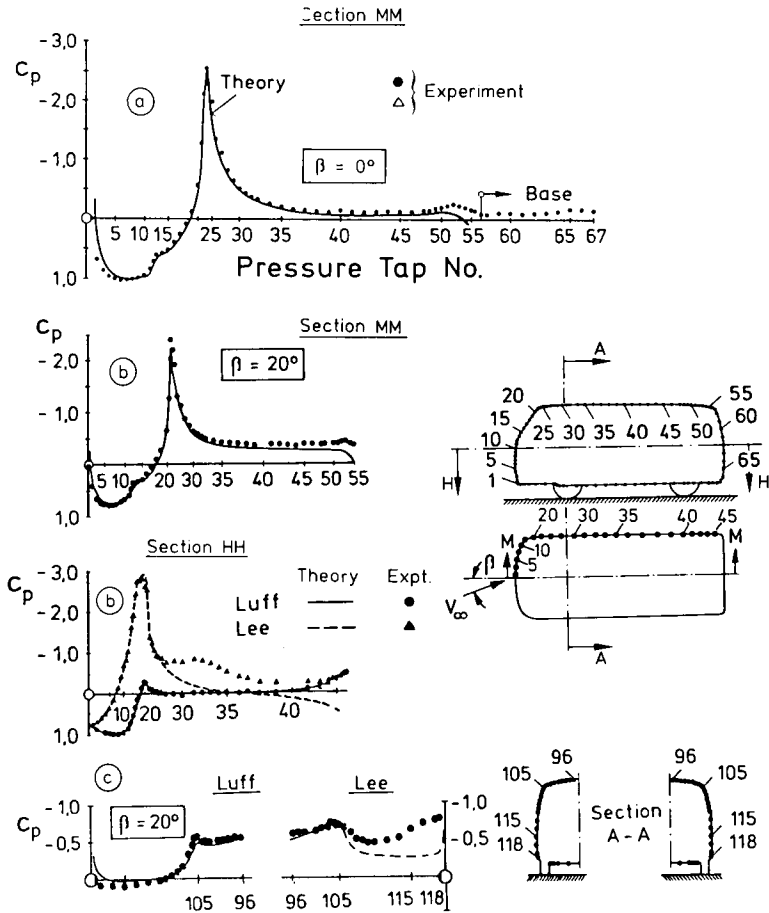


Figure 13.11 (a) Pressure distribution on VW van, longitudinal section without cross-wind. (b) Pressure distribution in longitudinal and horizontal sections with cross-wind ($\beta = 20^\circ$). (c) Pressure distribution in a transverse section AA, after ref. 13.8

only for attached flow, the pressure distribution on the van base, which is immersed in the separated flow of the wake, cannot be predicted. Considering the no-cross-wind situation ($\beta = 0^\circ$, Fig. 13.11a), the numerical and experimental results are in good agreement, except in the stagnation region and near the vehicle base. The deviation in the vicinity of the base is mainly due to inaccurate representation of the wake. The wake geometry was determined from photographs by illuminating the smoke-filled wake in the wind tunnel. Only a mean side and plan view of the wake was determined by this method.

Experimental results for flow with cross-wind represent a critical test for the theory as, under yaw, in addition to the flow separation at vehicle base, separation occurs also over parts of leeward surface. As was to be expected, a large discrepancy between computation and experiment is to be seen in the pressure plot of the horizontal section (Fig. 13.11b) and in

the transverse section AA (Fig. 13.11c). However, the pressure prediction on the windward side of these sections agrees closely with the experiments.

Using the same methodology, the inviscid flow field around a Mercedes C-111 research prototype car was computed by Ahmed.^{13.9} A surface geometry simulation of the vehicle, shown in Fig. 13.12 and employing

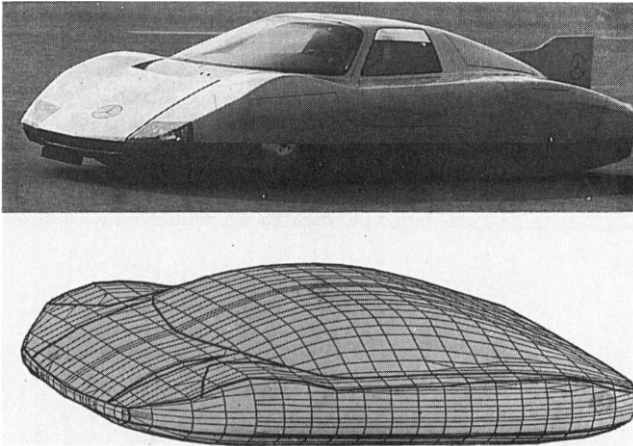


Figure 13.12 Mercedes C-111 research vehicle and its surface discretization, after ref. 13.9

1826 panels, exhibited the surface velocity distribution of Fig. 13.13. The pressure distribution shown in Fig. 13.14 for a tapered rear end version of the vehicle shows poor agreement between computation and experiment on the underside. Visualization of flow between model underside and ground plane showed extensive flow separation in the diffuser region formed by the rear of the model and ground.

An impressive demonstration of the complex surface details which can be handled by the panel method is illustrated in Fig. 13.15, which is due to Stricker.^{13.10} Surface discretization of this type is conveniently realized in an automobile manufacturing environment, where refined computer aided design systems (CAD) are available to design complicated surface geometries. As panel methods in principle place no restrictions on surface geometry, very realistic vehicle shapes, with the ensuing computer storage and time requirements, can be simulated. However, one has to bear in mind that the computed flow is an inviscid one; detailed reproduction of surface geometry is meaningful only as long as attached flow can be expected. Figure 13.15 illustrates the isobar plots for pressure on the vehicle surface for the zero cross-wind situation. Road surface has been modelled by fulfilling the flow tangency condition on its surface.

Losito et al.^{13.11} report results of panel method calculations for real shape car bodies and comparison with full-scale wind tunnel tests. The numerical model was without wheels, wheel arches, bumpers, mirrors and other surface projections. The underside of vehicle was a smooth plane surface. The complete surface of the body, i.e. including the base surface, was panellized. The numerical model was thus that of a closed body. Wind tunnel tests on full-scale configurations were done without engine and

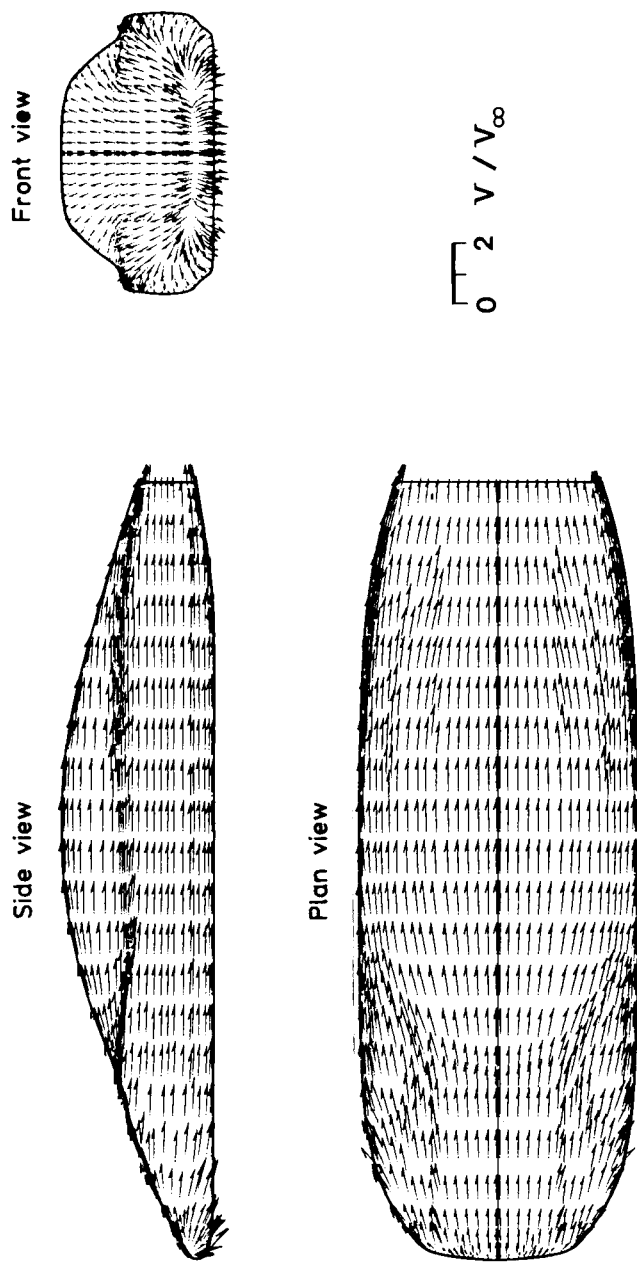


Figure 13.13 Computed velocity distribution on a Mercedes C-111 vehicle, after ref. 13.9

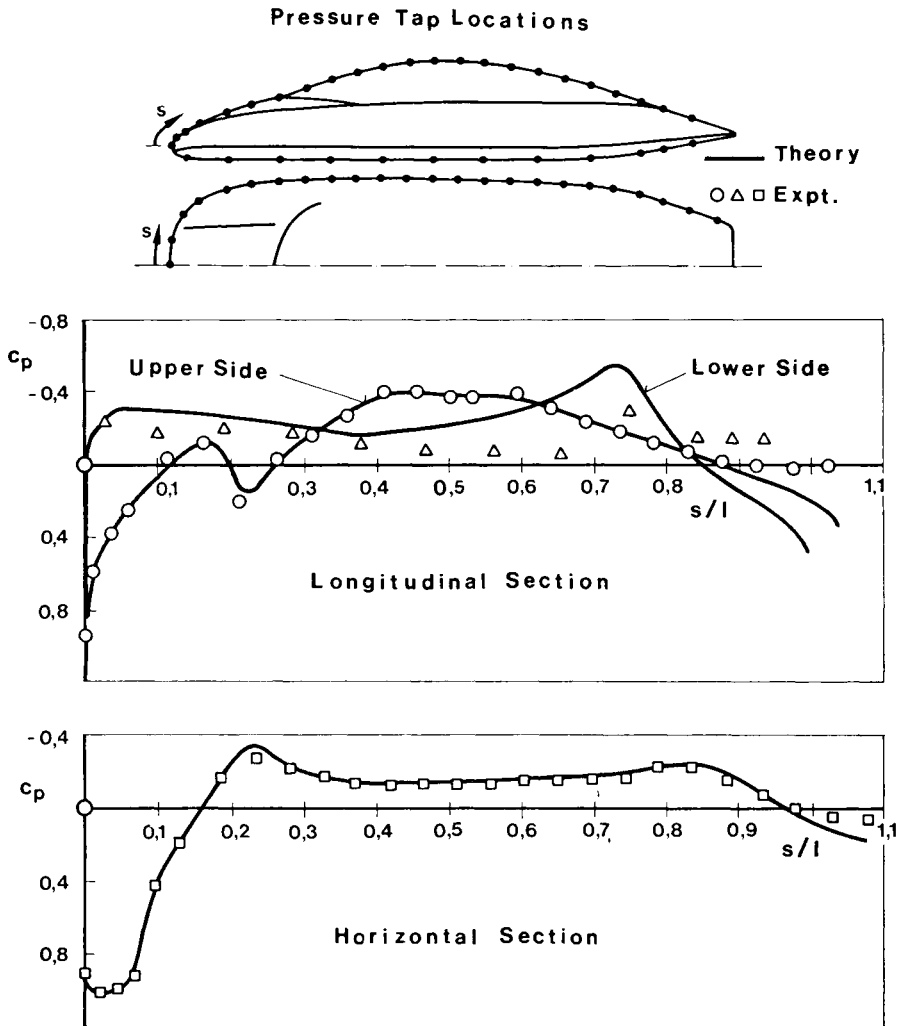


Figure 13.14 Comparison of numerical and experimental results, three-dimensional panel method; Mercedes C-111 vehicle, after ref. 13.9

passenger compartment flow present. Fig. 13.16 illustrates a typical result for a Fiat 124 passenger car under cross-wind flow conditions ($\beta = 15^\circ$). The nature of agreement between computed and experimental results is very similar to that already observed in Figs 13.11 and 13.14. The effect of 'closing' the body at the base leads to the sharp pressure peaks predicted at the base edge in the plane of symmetry and horizontal section. Also the computed base pressure, as was to be expected, bears no resemblance to the experimental results.

The application of the panel method to evaluate interference effects between two vehicles in the overtaking mode is investigated in ref. 13.8. The non-steady process has been treated as quasi-steady in the theoretical model. At two stages during the overtaking process, the pressure

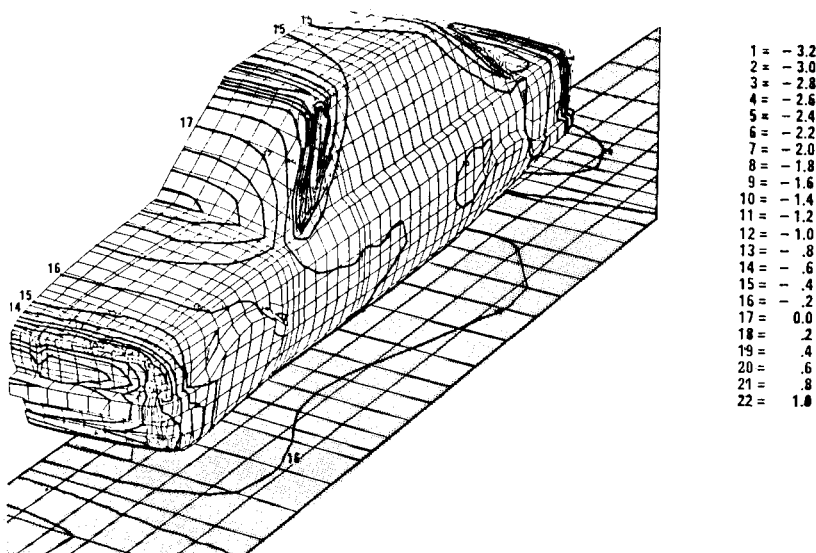


Figure 13.15 Surface discretization and computed isobars on a passenger car, after ref. 13.10

distribution on the inside flank of the overtaken vehicle is shown in Fig. 13.17. As the overtaken vehicle is approached, it experiences an anticlockwise turning moment about the vertical axis. When both vehicles are abreast, they are drawn towards each other.

A higher order panel method was applied by Stafford^{13.12} to a vehicle configuration to evaluate the flow field. The merits of using fewer panels with this scheme is coupled with the penalty of the complex numerics involved; this may, in adverse cases, obviate the advantage.

13.7.9 Non-linear inviscid flow methods

13.7.9.1 Solution of the Euler equations for incompressible flow

The main inadequacy of the inviscid incompressible (potential) flow treated in the previous section is that regions of separated flow, for example at the base of a vehicle, cannot be simulated. Also longitudinal vortices, which form at the A-pillar or at the side edges of the slanted base, are not predicted. To incorporate these real flow features in potential flow methods, at least kinematically, a phenomena modelling approach has to be employed. This may, for example, consist of discrete or distributed singularities, so arranged as to generate kinematically the flow in the 'separation' region. Plausible boundary conditions, derived from real flow physics, need to be imposed on this arrangement of singularities, whose strength and location in space can then be determined iteratively. The difficulties involved in this approach are the definition of proper boundary conditions, and advance knowledge of where and what type of phenomena modelling should be resorted to.

An interesting alternative to phenomena modelling is to consider the formation of the separation region (wake) as a time-dependent process.

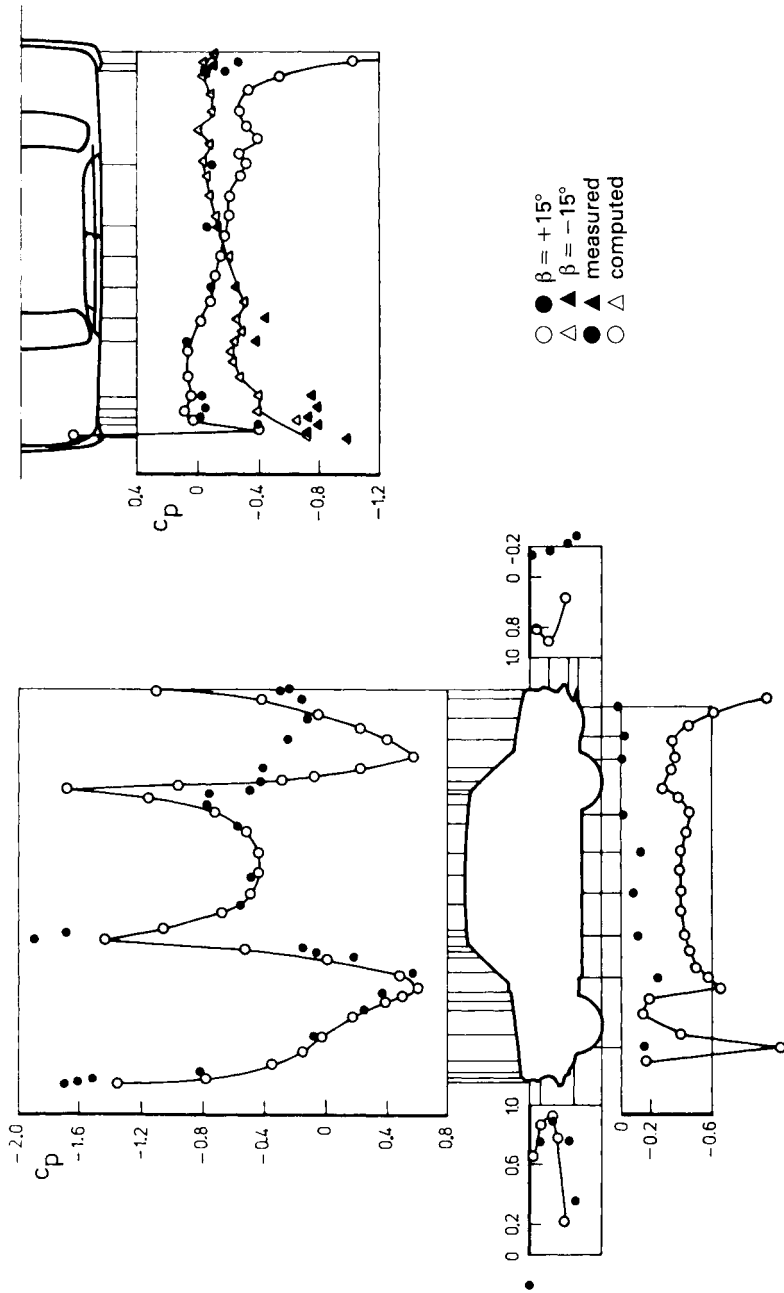


Figure 13.16 Comparison of three-dimensional panel method results with full-scale wind tunnel tests; Fiat 124 passenger car, after ref. 13.11

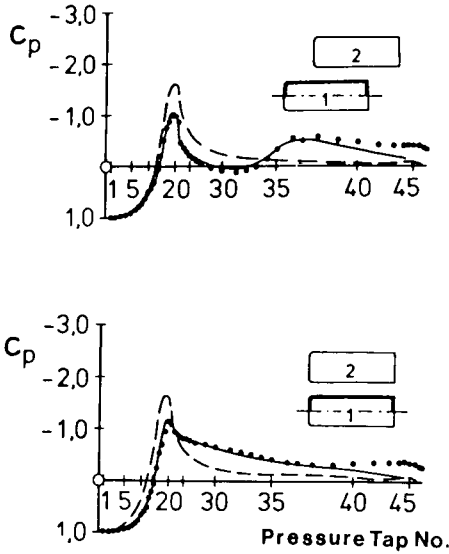


Figure 13.17 Variation of pressure on side flank of a vehicle during overtaking; VW van, three-dimensional panel method, after ref. 13.8

This method, proposed by Chometon,^{13.13} is based on the solution of the Euler equations for an incompressible, inviscid and unsteady flow (Eqn 13.17). The pressure terms in equation system 13.17 are eliminated by differentiating, for example, Eqn 13.17a with respect to y and Eqn 13.17b with respect to x . Subtraction of the two equations gives results in an equation free of pressure terms. Proceeding in a cyclic order with all three equations (13.17a, b and c), three further equations are obtained, which contain only terms of velocity components u , v and w . With rearrangement of the terms and introduction of the vortex vector \vec{W} ,

$$\vec{W} = \text{curl } \vec{V} \quad (13.72)$$

which, from Eqns 13.19 and 13.20, can be expressed as

$$\vec{W} = i \left(\frac{\partial w}{\partial y} - \frac{\partial v}{\partial z} \right) + j \left(\frac{\partial u}{\partial z} - \frac{\partial w}{\partial x} \right) + k \left(\frac{\partial v}{\partial x} - \frac{\partial u}{\partial y} \right) \quad (13.73)$$

one obtains the Euler equations as in ref. 13.13:

$$\frac{\partial \vec{W}}{\partial t} + (\vec{V} \cdot \nabla) \vec{W} - (\vec{W} \cdot \nabla) \vec{V} = 0 \quad (13.74)$$

Together with the continuity equation (Eqn 13.18), this system of equations represents a purely kinematic expression containing only the components u , v and w of the velocity vector \vec{V} . The boundary conditions which are imposed on the solution of Eqn 13.74 are

$$\vec{V} \cdot \vec{n} = 0 \quad (13.75)$$

and $\vec{V} \rightarrow \vec{V}_\infty$ for $\vec{r} \rightarrow \infty$

where \vec{n} denotes the surface normal vector, \vec{V}_∞ the velocity vector of the undisturbed flow, and \vec{r} the position vector. Physically the boundary conditions imply that the flow is tangential to the body surface, and the flow perturbation disappears as the distance away from body increases (see section 13.7.6).

The technique employed for solving Eqn 13.74 is, starting from an initial solution (which can be obtained by the panel method—see section 13.7.8), to obtain subsequent solutions after small time steps of Δt . To account for wake flow, for example at the side edges of the slanted base of a fastback

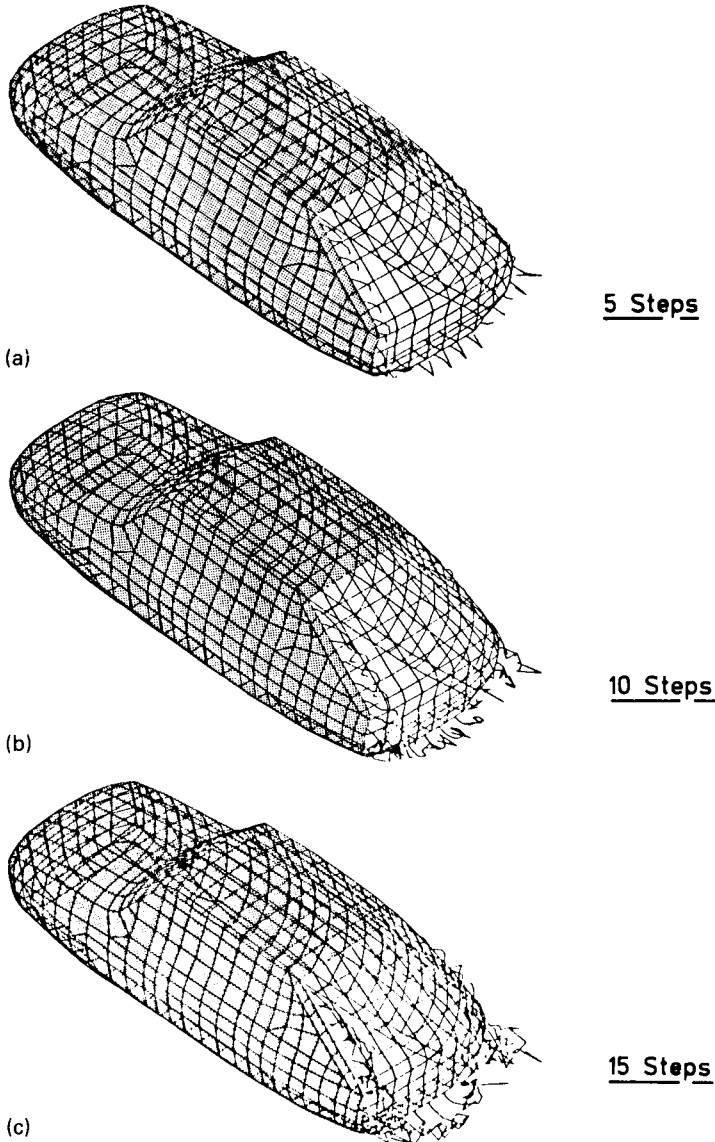


Figure 13.18 Wake simulation in inviscid flow. Development of wake after various time steps, after ref. 13.13: (a) 5 steps, (b) 10 steps, (c) 15 steps

car, vortex filaments are emitted from an assumed or known line of separation. As the time-stepping progresses, the length of the emitted discrete vortex filaments increases and these distort, due to the boundary conditions imposed, to form trajectories that show similarities to those observed in real flow. More details about how the strength of these vortices is determined and the discretization procedure are given in ref. 13.13.

Figure 13.18 depicts results obtained by Chometon on a Renault R20 automobile. The body surface was discretized by 375 plane panels, each overlaid with a dipole distribution, which is equivalent to the arrangement of a vortex filament around the panel periphery.

The separation line was assumed to be the perimeter of the rear end with the exception of the roof rear edge. Along this line, vortex filaments are emitted, which grow in length with each time step. Figures 13.18a, b and c show the development of the side edge vortex and the 'shear layer' roll-up at the lower edge of the vehicle base after 5, 10 and 15 time steps.

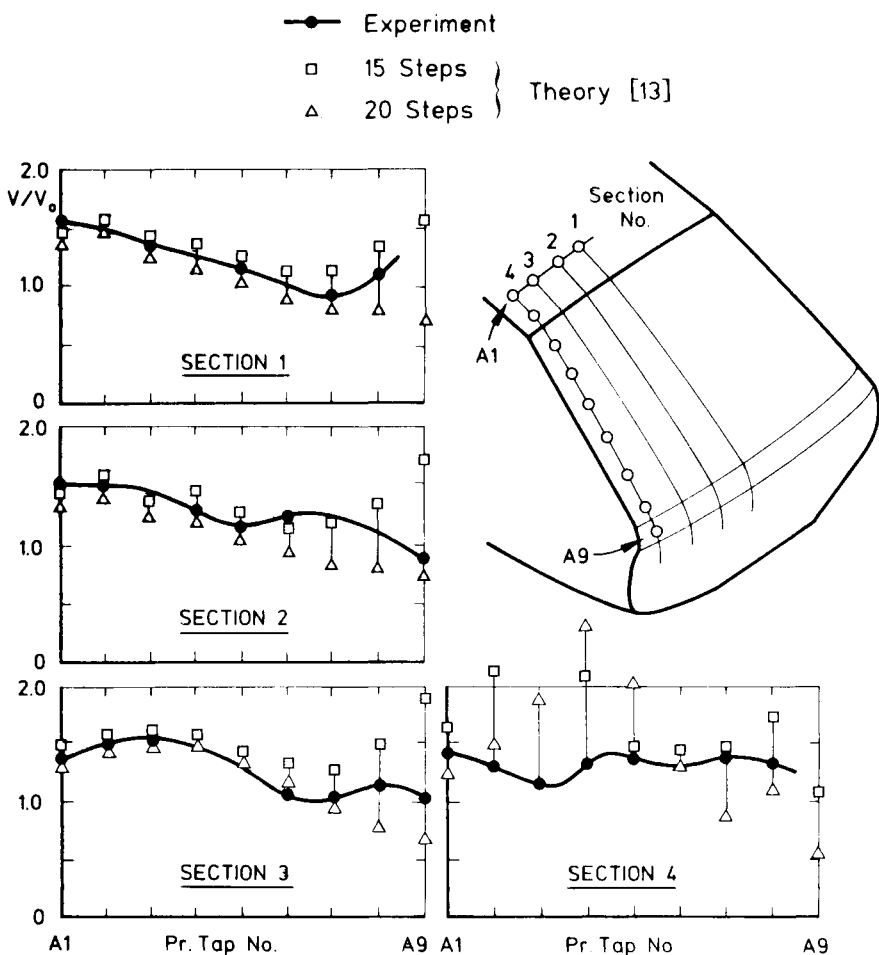


Figure 13.19 Comparison of computed and measured velocity on the slanted base surface, after ref. 13.13

Velocities computed on the slanted base surface with this technique are compared with experimental results in Fig. 13.19. Fair agreement is obtained in the mid area, becoming increasingly poor as the side edge or the trailing edge of the slant surface is reached. As visible in Fig. 13.18, with progressively increasing time steps and the coiling up of the vortex filaments, the stability of the numerical technique employed is endangered. Chometon mentions the introduction of a 'viscous core' concept to avoid these difficulties, which are an inherent characteristic of wake roll-up techniques employing discrete vortex filaments.

As shown in Fig. 13.18, the rear end surface of the vehicle is also represented. However, base pressure results obtained were, according to Chometon, not satisfactory.

13.7.9.2 Solution of the Euler equations for compressible flow

A promising feature of the non-linear inviscid methods being developed for aeronautical use is claimed by the developers of these codes to be the inherent ability to simulate regions of 'separation' such as those mentioned above. The governing equations for these methods are the inviscid compressible Euler equations in the time-dependent form.^{13,14} These are a system of non-linear partial differential equations of hyperbolic type.

Regions of separation in real flow are characterized by a non-zero value of circulation. The mechanism of generation of circulation in the solutions of compressible Euler equations is explained as follows^{13,15} (see also ref. 13.16).

The marching coordinate for solving the time-dependent Euler equations being the time t , the procedure involves a number of time steps. After this transient phase, a converged solution is obtained, which is accepted as that describing the steady state. During the transient phase, the inviscid compressible flow creates a shock, with an accompanying entropy production, at sharp corners or at points where abrupt contour changes take place. This entropy production generates flow kinematics bearing strong similarity to that observed in separation regions of real flow.

Another explanation, also offered elsewhere, is that to make the underlying system of equations numerically stable, 'artificial viscosity' terms are introduced in the codes which are in current use. These then produce the observed circulation.

It is unclear however how far, with the introduction of these terms, the governing equations can still be termed Euler equations and whether their hyperbolic character remains unchanged. Even if the introduction of artificial viscosity is so conditioned that it is effective only during the transient phase and its influence diminishes with the solution converging to steady state, it must be made clear what system of equations is being solved to start with, and what effect a progressively changing governing system of equations can have on the final solution.

These considerations may be of less interest to users primarily concerned with the actual predictive capability of these codes. Bearing in mind that the codes treat air as being compressible, the question arises, from the viewpoint of a vehicle aerodynamicist, how these methods could be applied to the very low Mach number flows. Progressive decrease in Mach number

invariably leads, in the existing codes, to analytical and numerical difficulties (see ref. 13.17). To circumvent these, it may be necessary to introduce artifices such as 'artificial compressibility' terms. The impression one gains is that, even though these approaches signal significant advances in computational fluid dynamics as far as aeronautical applications are concerned, the physics involved is not sufficiently understood to enable a straightforward extension to the incompressible, separation-dominated vehicle flow fields.

An example of a two-dimensional Euler equations solution, of interest to vehicle aerodynamicists, is that of a backward facing step, reproduced from the work of Schmidt et al.^{13.15} in Fig. 13.20.

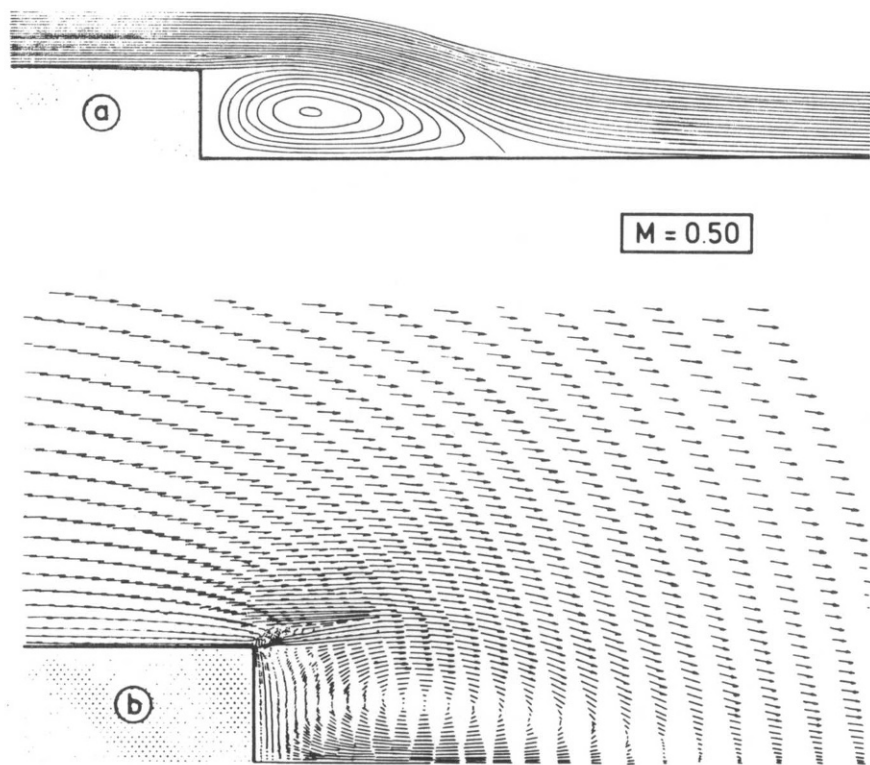


Figure 13.20 (a) Streamlines, and (b) velocity distribution for a backward-facing step. Two-dimensional Euler equation solution results from ref. 13.15

The velocity vector plot for the Mach-number of 0.5 clearly indicates a region of separated circulatory flow behind the step—as is commonly observed in a real flow. A comparison with experimental data, especially for very low values of Mach number, is not available. The results of Fig. 13.20 are thus essentially of a qualitative nature. Three-dimensional solutions for Euler equations around vehicle bodies have not yet been published.

13.8 Coupled inviscid flow—boundary layer methods

The classic approach when considering viscous effects in attached high Reynolds number flow is to view them as confined to a thin boundary layer in the vicinity of body surface. The governing equations for the flow in this layer are the so-called boundary layer equations, which represent a simplification of the Navier-Stokes equations (see ref. 13.1). Outside this viscous layer, the flow is considered to be inviscid. The main effect of the viscous boundary layer is a retardation of the flow in surface proximity, with the velocity becoming equal to zero on the surface itself ('no slip' condition). Compared to the inviscid flow around the body, the boundary layer in the real flow appears to displace the inviscid flow outwards and away from body surface.

The usual approach is first to perform an inviscid computation for the flow on the body surface, using, for example, the panel method. The pressure, velocity and streamline data obtained on the body surface is assumed to exist slightly above the body surface, i.e. outside the boundary layer. With this as input, a boundary layer code is employed to compute the boundary layer and displacement thickness. Using an equivalent source or displacement thickness concept to account for the boundary layer, a new inviscid calculation is then done. This iterative process is repeated till no significant change in the computed boundary layer values is present.

However, the artifice of equivalent source to create the boundary layer displacement effect is preferable, in the attached flow regime, to the displacement thickness concept, because the latter involves a new geometry generation after each iteration step in the panel method program and consequently more computational effort. The equivalent source concept involves the arrangement of a source distribution on the body surface which is so determined that it 'pushes' the inviscid flow away from body surface by an amount equal to the local displacement thickness.

Subdivision of the flow field into a viscous boundary layer and an inviscid flow region implies a weak interaction between the two flow regimes. This may be justified in regions of attached flow and weak transverse flow gradients, but is inadequate in the wake region of a vehicle flow field. Losito et al.^{13,11} have applied a simplified approach when considering the boundary layer effects on a car body. Instead of using a three-dimensional boundary layer code, they apply a two-dimensional boundary layer method along three-dimensional streamlines obtained through an inviscid (panel method) calculation.

Investigation of integral and finite difference methods of calculating the boundary layers in ref. 13.11 show that, even though the displacement thickness obtained by both methods is about the same, momentum thickness and friction coefficient are generally overestimated by the integral methods. Losito et al. state further that, with their approach, realistic prediction of separation was possible only by using a finite difference scheme for the boundary layer calculations. An illustrative example of this effect is shown in Fig. 13.21 for a Fiat 124 car.^{13,11} The separation line predicted by the finite difference scheme agrees with the experimental results, whereas the integral boundary layer method indicates a more downstream location of the separation line.

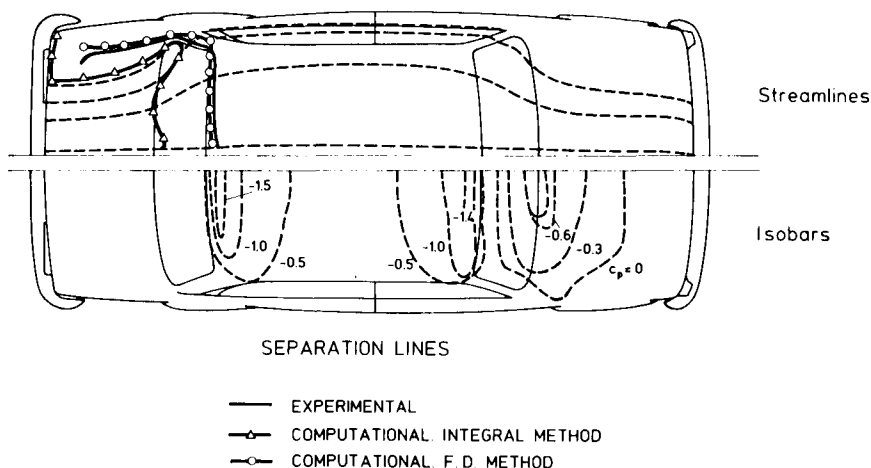


Figure 13.21 Potential isobars and streamlines—computed and experimental separation lines for a Fiat 124 (top view), after ref. 13.11

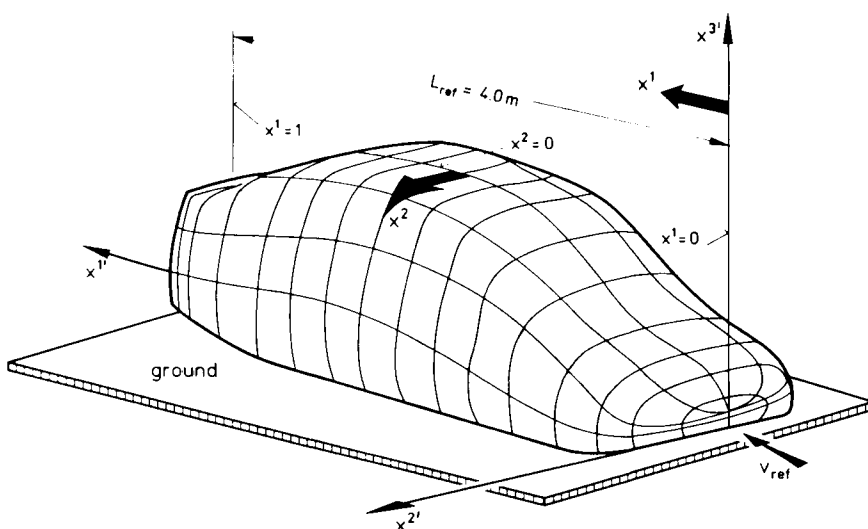


Figure 13.22 Schematic of body surface coordinates x^α ($\alpha = 1, 2$), and Cartesian reference coordinates $x^{i'}$ ($i' = 1, 2, 3$), after ref. 13.19

Bretthauer^{13.18} and Hirschel^{13.19} applied a three-dimensional turbulent boundary layer integral method to evaluate the boundary layer development over simplified ground vehicle type bluff bodies. Figure 13.22, reproduced from ref. 13.19, illustrates schematically the surface discretization and the body-centred coordinate system used, which is described in more detail in ref. 13.20.

Figure 13.23 shows the distortion of the surface streamlines (dotted) caused by the boundary layer for the automobile-like body.^{13.19} The tendency of the flow to separate is indicated by the convergent behaviour of the (dotted) streamlines on the upper rear end surface. It is important to

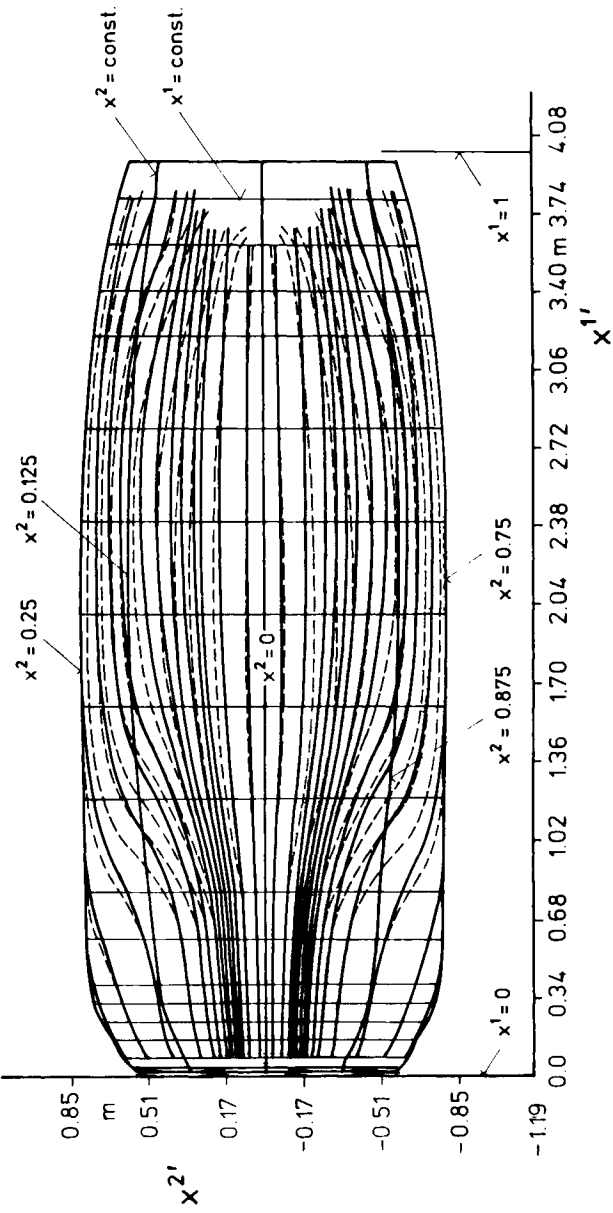


Figure 13.23 Streamlines at the edge of the boundary layer (—) and on the body surface (-----), after ref. 13.19

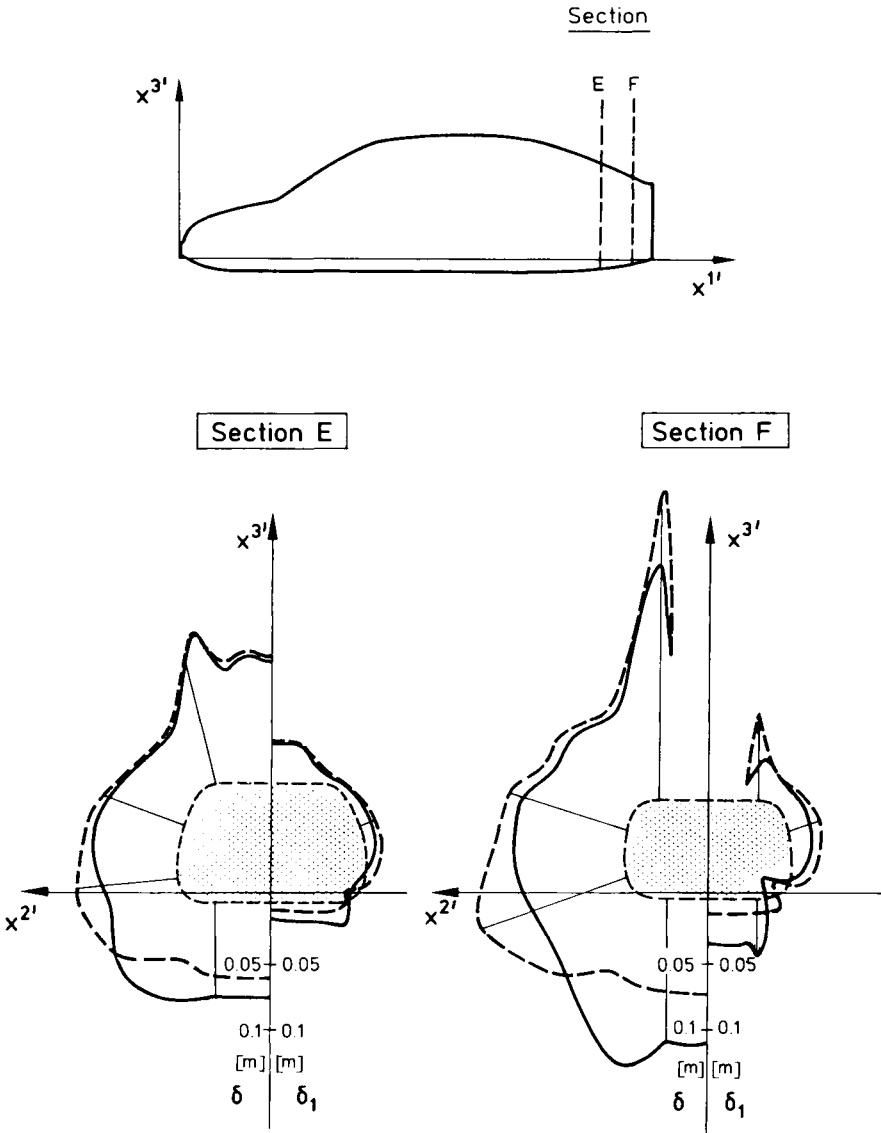


Figure 13.24 Distribution of computed boundary layer δ and displacement thickness δ_1 over the body contour, with and without ground, after ref. 13.19

note that, since the wake at the vehicle base is not simulated, an interaction between wake flow and body flow is not considered in the flow calculation. Thus a separation line, evaluated as the locus of points where the wall friction tends to zero, may not represent the actual situation of a real flow. The results obtained serve as a guide to localize regions of flow separation.

Also shown in Fig. 13.24 is the effect of the ground on boundary layer development. Mainly the rear part and undersurface of the body are influenced by the presence of the ground; a thicker boundary layer is computed on the undersurface with ground simulated. A bulge near

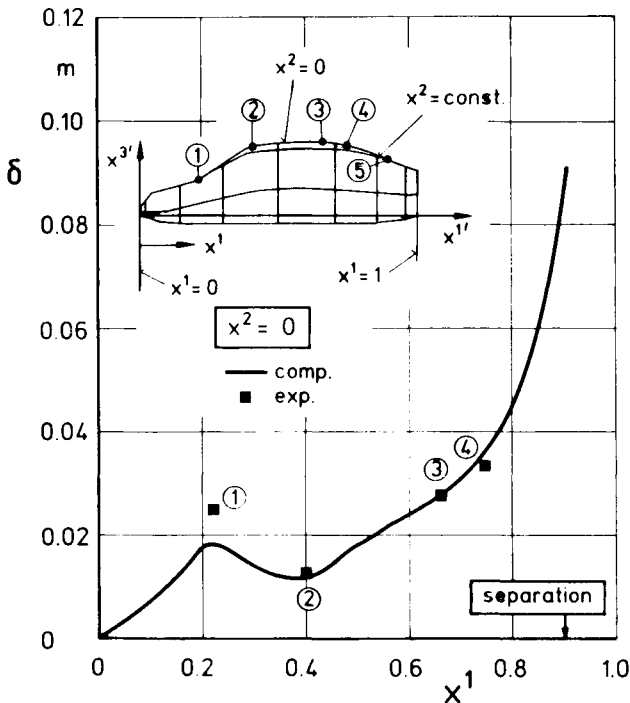


Figure 13.25 Measured and computed boundary layer thickness on the body upper surface, in the plane of symmetry, after ref. 13.19

roof/side flank and side flank/undersurface edges indicates a separation tendency with vortex formation.

Figure 13.25 illustrates a comparison of the computed boundary layer thickness with the experimental data obtained on a full-scale wind tunnel model. Computations were done for a body length based Reynolds number of 9 million. Experiments done in the Reynolds number range of 7.5 to 12.6 million were corrected to correspond with the computations using the $1/7$ power law representation of the boundary layer velocity profile. The theoretical boundary layer thickness results agree reasonably well at three stations on the upper surface centre line, but deviation is noticeable at the foot of the windscreen. Some explanation of this behaviour is offered in ref. 13.19.

Losito^{13.11} and Hirschel^{13.19} have attempted to calculate the total drag of the vehicles they considered by making simple assumptions about the base pressure in the region of separated flow. The results are however to be considered as of a preliminary nature.

An improvement on the approaches discussed above has been proposed by Summa and Maskew.^{13.21} A panel method is iteratively coupled with an integral boundary layer code. The wake at the vehicle base is simulated by enclosing it with a doublet sheet in a similar fashion to that done by Ahmed and Hucho in ref. 13.8. The wake surface emanated from an assumed separation line on the body surface. The shape of this wake surface is determined iteratively by requiring it to be a stream surface. In the actual

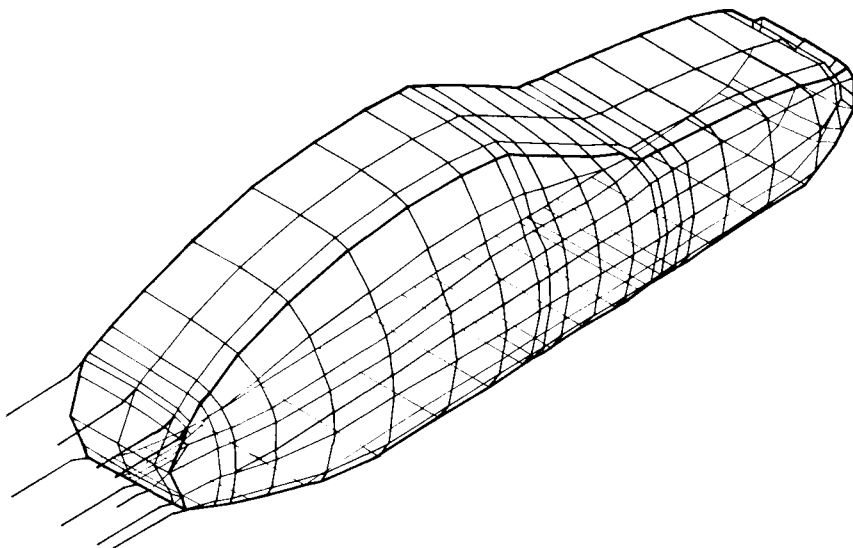


Figure 13.26 Surface discretization and wake simulation for a Porsche 924 vehicle, after ref. 13.21

computation, the wake surface is left open after a certain downstream length; this is stated to have little effect on the results.^{13.8} The boundary layer displacement is accounted for by the previously mentioned technique of 'equivalent sources' placed on the surface.

Following the panel method solution, the surface streamlines are traced from the computed surface velocity distribution. The boundary layer is calculated along each streamline, first as laminar and then, after transition, as turbulent. Turbulent boundary layer separation on a given streamline is

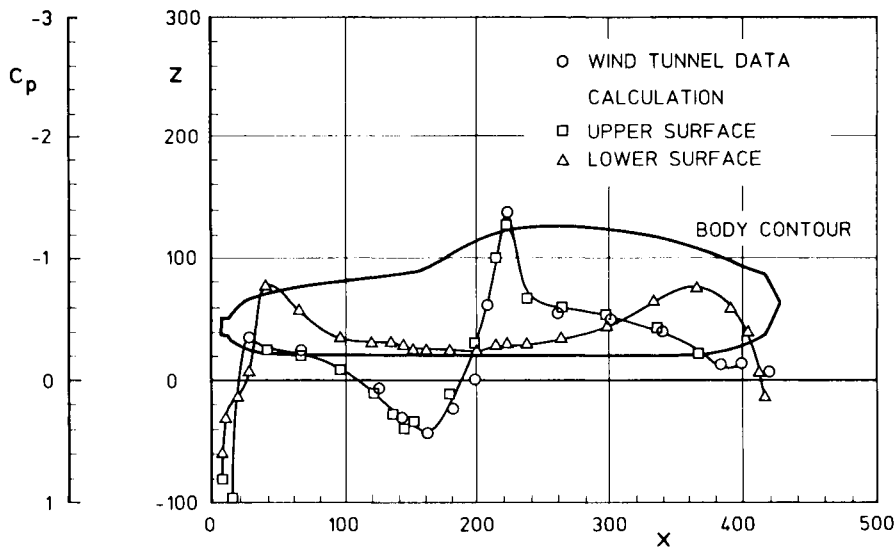


Figure 13.27 Comparison of numerical and experimental pressure distribution in the plane of symmetry for a Porsche 924, after ref. 13.21

predicted when the value of skin friction reaches zero. The location of the separation line is considered to be the locus of these separation points. As the iteration proceeds, the location of the separation line may shift, which means that the location of the doublet sheet representing the wake has to be adjusted accordingly.

The results obtained in ref. 13.21 for a simplified Porsche 924 automobile are shown in Figs 13.26, 13.27 and 13.28. The surface

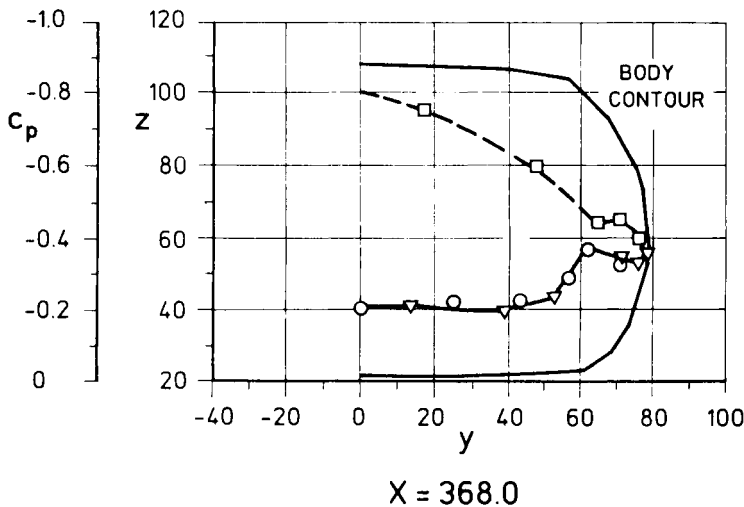
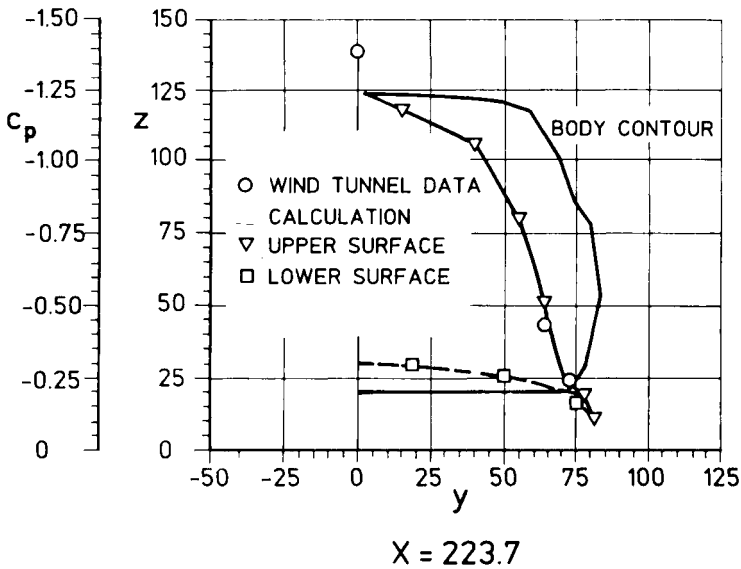


Figure 13.28 Comparison of numerical and experimental pressure distribution over the body contour at two transverse sections of a Porsche 924 vehicle, after ref. 13.21

discretization and wake representation of the vehicle is depicted in Fig. 13.26; in all, 314 panels were used on the half-body and 156 panels on the wake. Ground simulation was provided by the image technique. Wheels and surface details were not represented in the numerical model. The rear end of the body, as indicated in Fig. 13.26, was also discretized, so that a pressure prediction on this surface, wetted by the wake, is in principle possible. The wake geometry was prescribed in the computations.

In Fig. 13.27 the computed pressure distribution in the longitudinal central plane is compared with full-scale experimental results. Except for a slight underestimation of peak suction at windscreen/roof junction, the agreement is good, especially so in the vicinity of the rear end. No experimental results are available for the body undersurface. The experimental results indicate that over the body centreline attached flow prevailed up to the rear end, which may, at least in part, be responsible for the close agreement obtained.

Figure 13.28 illustrates the comparison of the predicted pressure distribution and experimental results over two transverse sections. Here again the agreement between the two results is exceptionally good.

Good results obtained by the method of ref. 13.21 for the Porsche 924 vehicle, as the authors also state, are not necessarily representative of other vehicle shapes. More refinement of wake simulation is needed to improve the prediction capability of this promising approach.

13.9 Methods based on solution of Navier-Stokes equations

The Navier-Stokes equations (see ref. 13.1) for a homogeneous, incompressible medium, together with the continuity equation, can be used to describe adequately the *laminar* flow around a road vehicle. As these equations represent, in principle, all the physics involved, no additional assumptions and modelling, as in the methods of preceding sections, are needed.

However, the flow around actual road vehicles is mainly *turbulent*, and Navier-Stokes equations for turbulent flows need a turbulence 'model', to make the system of equations amenable to numerical analysis. The basic equations employed are averaged over a time interval. This interval is chosen so as to make the equations independent of the random eddy fluctuations, yet permit a resolution of the unsteady macro-structures which may be present.

The main problems encountered are of turbulence modelling and of finding a suitable numerical solution scheme. Much attention is currently devoted to the modelling of turbulence but models of sufficient generality and applicable to complex flows—such as around bluff vehicle type bodies—are not yet available.

The method often used to solve the Navier-Stokes equations in aeronautical practice is the finite difference technique. According to this approach, the Navier-Stokes equations are discretized in a domain around the body into a set of finite difference equations. The flow region itself is partitioned by overlaying it with a cartesian grid. In this grid the solution of the discretized equations is sought iteratively through standard solution

techniques. The irregular shape of a road vehicle does not allow proper representation through a rectangular grid, so that in the numerical representation the grid lines cannot be made to coincide with the body contour and consequently the surface of the vehicle is serrated. Obviously this is a drawback. As is well known, seemingly insignificant surface details can trigger major changes in the overall vehicle flow field. To improve the body surface representation, a special treatment of the near-wall flow region is therefore necessary.

Haase^{13.22} used the finite difference technique to solve the *laminar* steady Navier-Stokes equations for the flow around a basic road vehicle like body. His results, quoted in refs 13.10 and 13.16, are reproduced in Figs 13.29 and 13.30. Figure 13.29 illustrates the grid of $55 \times 25 \times 35$ ($= 48\,125$) points arranged in one half of the cartesian computation domain around the vehicle. To achieve sufficient resolution a denser grid is employed near the body surface, in regions of high curvature and in the

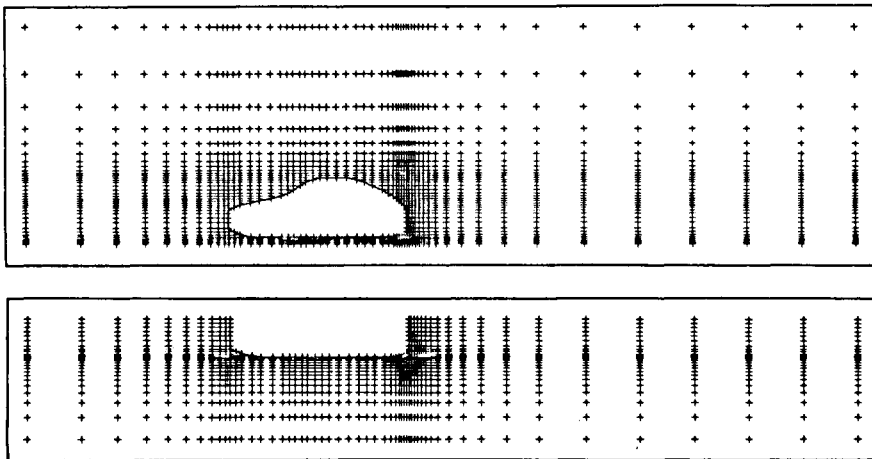


Figure 13.29 Computational grid for the laminar three-dimensional Navier-Stokes equations solution, after ref. 13.22

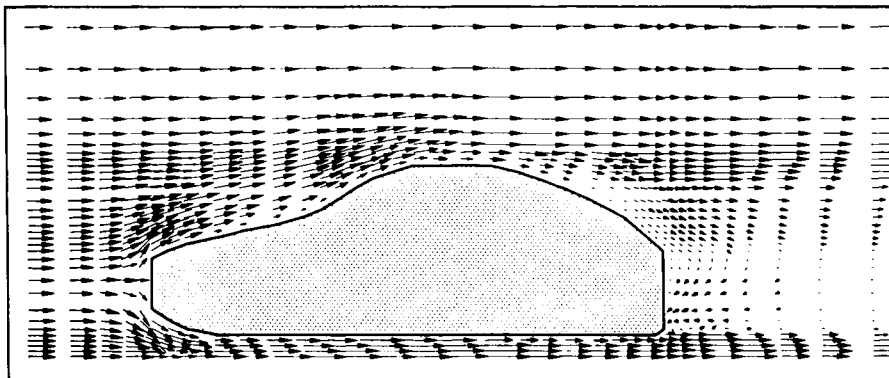


Figure 13.30 Velocity distribution in the plane of symmetry; solution of three-dimensional laminar Navier-Stokes equations, after ref. 13.22

wake. This density of the grid needs to be retained over the computation domain, even when a finer resolution of flow details further away from body surface is not of prime interest. The demands on computer storage and time are consequently high.

Figure 13.30 depicts the velocity distribution obtained in the longitudinal central plane. Retardation of flow in the vicinity of the base and the formation of recirculation zones are visible. The region of retarded flow behind the vehicle is apparently much longer than that observed in real flow (see ref. 13.23).

Demuren and Rodi^{13.24} presented a finite difference solution of the three-dimensional, *turbulent*, time-averaged steady Navier-Stokes equations for the flow over an idealized notchback type of vehicle. (Results of a two-dimensional calculation for a fastback type of vehicle are also presented in ref. 13.24. The authors state that comparison of the numerical results with measurements at the central plane of a three-dimensional model show that essential features of the flow are not captured by a two-dimensional treatment of the problem.) The method uses a cartesian grid so that the inclined vehicle contour is approximated by steps (Fig. 13.31). Closure of the system of equations was obtained by using the k - ϵ turbulence model of Rodi^{13.25} (see also ref. 13.26). The car half-body

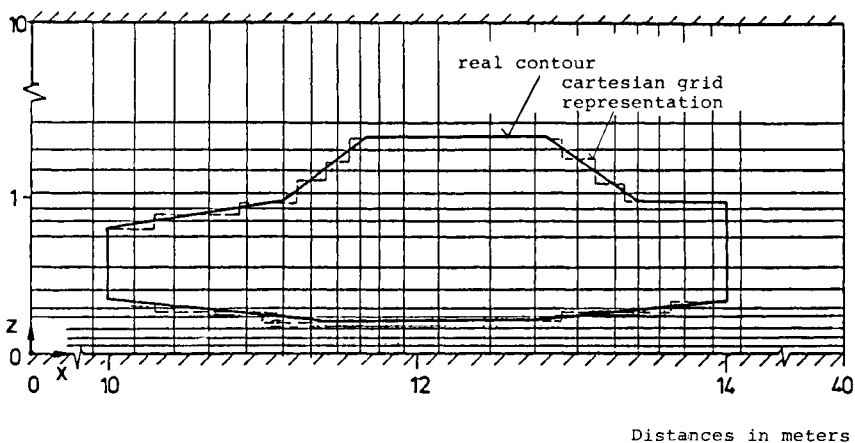


Figure 13.31 Body contour discretization with a Cartesian grid; solution of three-dimensional turbulent Navier-Stokes equations, after ref. 13.24

considered is enclosed in a box-like computational domain. This consists of top, side and bottom 'wind tunnel walls' as well as an inflow and outflow plane. Together with the plane of symmetry, boundary conditions are specified for the dependent variables in these six planes. As mentioned above, due to the step-like numerical representation of the body surface, a special wall-function procedure is employed for the near-wall region. More details of the boundary conditions imposed are given in ref. 13.24. The computational grid had $45 \times 26 \times 17$ ($= 19\,890$) points distributed in the x , y and z directions.

Figure 13.32 presents results of the computed velocity distribution,^{13.24} in three x - z planes. The enlarged representation of the computed flow in

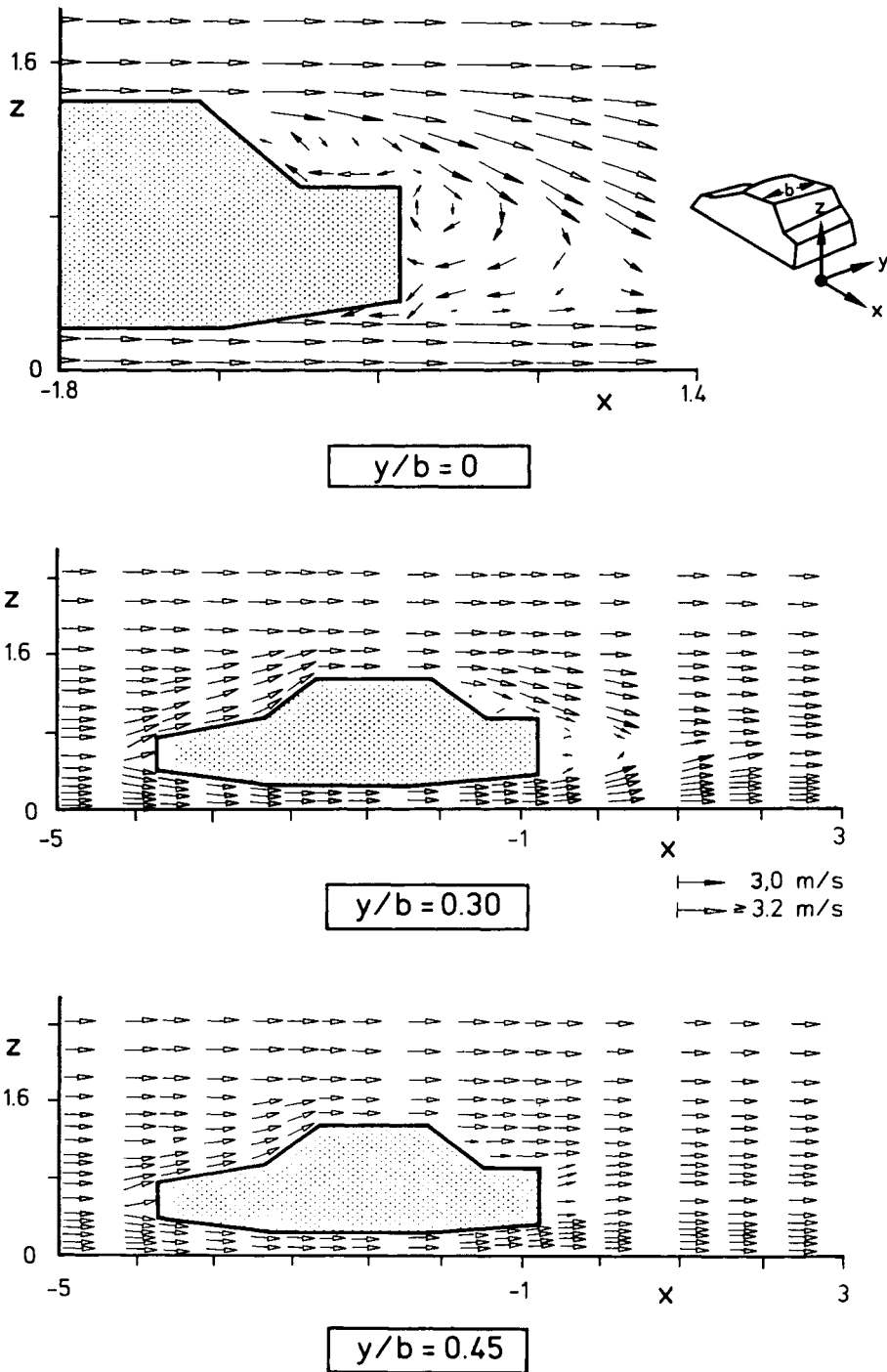


Figure 13.32 Velocity distribution in longitudinal planes; solution of three-dimensional turbulent Navier-Stokes equations, after ref. 13.24

the plane of symmetry shows separation from the roof and the boot rear edge. A circulatory flow region forms over the boot and another, with the same sense of rotation, behind the upper edge of the flat base. The reverse flow obtained on the upswept rear undersurface is probably incorrect. The length of the separation bubble at the vehicle base, at both stations $y/b = 0$

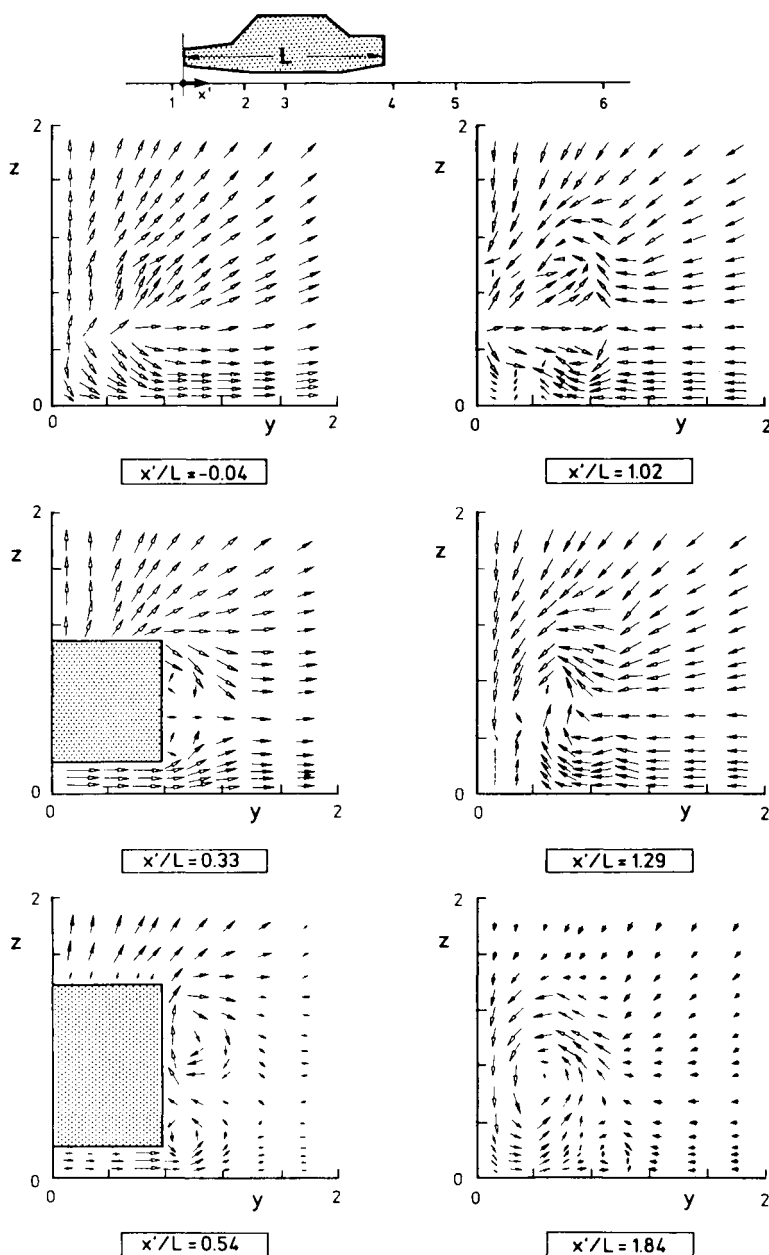


Figure 13.33 Cross-flow velocity distribution in various transverse planes; solution of three-dimensional Navier-Stokes equations, after ref. 13.24

and 0.3, appears to be the same, indicating a weaker simulation of three-dimensional effects in the lateral direction. Also the flow near the rear window, at station $y/b = 0.45$, deviates from the real flow behaviour (see ref. 13.23).

The series of results shown in Fig. 13.33 (reproduced from ref. 13.24), illustrates the macro-structure of the cross-flow developing around the vehicle. Outward displacement of the flow in the front sections and formation of vortices on the side flank up to $x/l = 0.54$ can be observed in the velocity vector plots. The transition of the cross-flow downstream of this station cannot be inferred from the data presented.

Using a finite difference scheme developed by Patankar and Spalding,^{13.26} Markatos^{13.27} computed the flow field around a vehicle body of notchback type. The iterative solution procedure used to solve the time-averaged Navier-Stokes equations for steady flow is similar to that of Demuren and Rodi.^{13.24} The results presented by Markatos, with only $15 \times 9 \times 25 (=3375)$ grid points in the computation domain, serve mainly to demonstrate the basic capability of the approach. A sample result, Fig. 13.34, shows the pressure isobars, computed at a y - z plane just

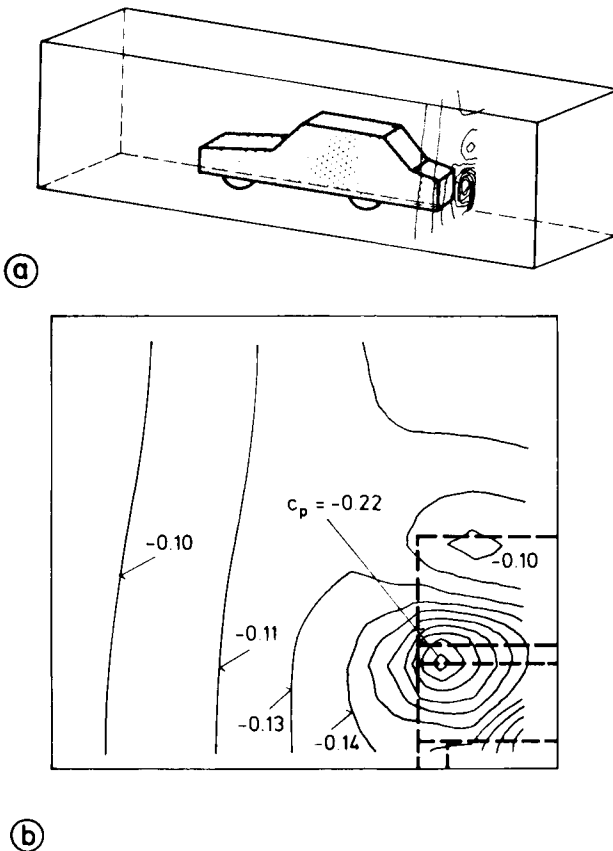


Figure 13.34 (a) Computation domain and (b) isobar plot for a notchback vehicle; solution of three-dimensional turbulent Navier-Stokes equations, after ref. 13.27

downstream of the body. Some qualitative similarity to the real flow situation can be observed.

The results obtained by the solution of Navier-Stokes equations, as shown in Figs 13.30, 13.32, 13.33 and 13.34 show that the macro-structure of the complex three-dimensional turbulent flow around a car-like body is qualitatively correctly simulated. Separation and the formation of longitudinal vortices is indicated and bears similarity to the phenomena observed in real flow. Due to lack of available data, it is difficult to make a statement about the quantitative accuracy of the prediction but it does not seem to be very high. Inadequacies of the turbulence model, the coarse grids used, inaccurate representation of body contour, inadequate boundary condition in the near-wall region, and other factors, lead to results which differ, even qualitatively, from real flow behaviour. Both Demuren and Markatos note that the numerical accuracy of the results or the results themselves may vary with grid refinement.

Results for vehicle flow fields, using time-dependent Navier-Stokes equations, are not available in the open literature. Computations employing the finite volume technique have appeared since the time of writing: see refs 13.28, 13.29.

13.10 Concluding remarks

Many of the numerical methods treated in the preceding sections are used routinely as design tools in the aerospace industry. Similar success has not yet been achieved in their application to the computing of vehicle flow fields. No calculation scheme is presently available which can both qualitatively and quantitatively describe the real flow field around even a basic vehicle-type body. One of the reasons for this was the less pressing need in the past, on the part of automobile manufacturers, to apply these techniques in the design of automobiles and utility vehicles. On the other hand, aerodynamicists engaged primarily in design of aircraft had sufficient margins in shape design to avoid or minimize separation and thus were less concerned with the physics of such flows. The majority of the computational techniques developed for aeronautical use are based on the premise of attached flow.

Linear inviscid flow methods, such as the panel method, very often constitute the first step in the computation of a vehicle flow field. The main advantage of the panel method is its extreme flexibility to represent complicated and realistic body geometry with relatively modest effort. At present this capability is unsurpassed by other numerical methods. The computation effort is, compared to other techniques, also small. One of the main reasons for this is that only a discretization of body surface is needed in the panel method approach. As often pressure and velocity distribution on body surface alone are of interest, the computational effort is directly related to this objective. In other methods, such as solution of Euler and Navier-Stokes equations, the whole flow domain around the body has to be discretized. The solution delivers a large amount of data, even for regions far away from body surface. In a parametric design study, the computation of this far field, which is of less interest, amounts to a penalty.

The major limitation of the panel method is that it can simulate only attached flow. Separation, at least kinematically, has to be considered by phenomena modelling. This involves a vast experimental basis to model correctly the separated flow macro-structure, for example in the wake of a vehicle. As the panel method does not compute the pressure in the separated flow regime, prediction of the pressure drag is not possible. Unless suitable modelling is employed in the computation scheme, interaction effects, such as between attached flow and the wake, remain unconsidered. A reasonable prediction of lift experienced by a vehicle is, however, possible by the panel method even in the absence of a refined separated flow modelling.

On a short-term basis, the coupled panel method/boundary layer computation schemes combined with refined phenomena modelling of the vehicle wake have the chance of maturing into cost-effective design tools. Much of the success of this approach depends on how well the vortical and 'separation bubble' type of wake phenomena are modelled.

The status of the boundary layer computer codes currently available is that they fail near the region of flow separation. Lines of flow separation can be determined only approximately in view of the complex nature of three-dimensional flow. The flow data at these 'separation' lines is of some help in modelling the separated flow regions. In the attached flow regime, the boundary layer computations enable an estimation of the friction drag. However, for vehicle-type bodies, this accounts for only a small portion of the total drag. The more realistic surface streamlines resulting from such a calculation are helpful in proper location of ventilation vents and in the analysis of rainwater flow, dirt accumulation etc. on the vehicle surface. As the coupled panel method/boundary layer codes are also unable to predict pressure in the separation zone, a rational basis to evaluate the pressure drag, and thus total drag, is at present not available.

Non-linear inviscid flow schemes, based on the solution of compressible Euler equations, avoid the need for phenomena modelling. This very significant advantage, based on results obtained with aeronautical configurations, needs substantiation for the incompressible vehicle flow problems. The analytical and numerical aspects of this approach are in process of rapid development.

By treating the medium of air as inviscid, solutions of the Euler equations do not include viscous effects such as boundary layer displacement, total pressure loss etc. These results therefore need to be corrected with a boundary layer code. The question which arises is how far this approach then remains short of a solution of the full Navier-Stokes equations.

The Navier-Stokes equations represent, in principle, the true simulation of the physics of viscous flow. The main drawback of the methods currently employed to solve these equations is the cartesian grid, which allows the body contour to be only crudely represented. Special treatment of the near-wall region limits the generality and can introduce incorrect physics in the computed flow. A body-centred grid may bring improvements in the discretization.

Finite volume techniques to solve the Navier-Stokes equations avoid the disadvantages of a cartesian grid and are flexible in the generation of a

general body contour. The key problem of turbulence modelling remains open, however, irrespective of which of the two solution procedures mentioned above is adopted. A long-range effort is necessary before appropriate turbulence models for vehicle-type flow fields become available. Solutions of three-dimensional Navier-Stokes equations, employing the finite volume technique to compute vehicle flows, have been reported only recently.

With the provision of a correct turbulence model, the Navier-Stokes equations describe completely the physics of the viscous flow. Accuracy of the prediction is then basically dependent on grid density. As the present numerical schemes have to retain this grid density over a major portion of the computation domain, the computation effort becomes very large. Use of Navier-Stokes solutions must therefore remain restricted to investigations in a late design stage, when more detailed information may be required.

13.11 Notation

| | |
|--|--|
| A_{ij} | component of a_{ij} normal to surface of element i |
| A_{qi}, B_{qj} | influence coefficients, (Eqn 13.69) |
| F_i, F_p, F_v | inertial, viscous and pressure force |
| M, Ma | Mach number |
| M, M_p | strength of a point or plane doublet (Eqns 13.45, 13.48) |
| Q | source strength or volume (Eqn 13.39); also a point in flow field |
| R | radial coordinate in spherical coordinate system |
| $Re = \frac{Vl}{\nu}$ | Reynolds number (Eqn 13.8) |
| R_i | component of onset flow normal to surface of element i |
| S_B, S_W | body and wake surface |
| \vec{V}, V | velocity vector and its magnitude |
| $\vec{V}_\infty, \vec{V}_p$ | onset flow and perturbation flow velocity vector (Eqn 13.57 and Fig. 13.9a) |
| \vec{W} | vortex vector (Eqn 13.73) |
| X_j, Y_j | dimensionless source/sink or doublet strength of panel j |
| a | speed of sound |
| $a_1, a_2 \dots$ | constants (Eqn 13.26) |
| a_{ij} | velocity induced by a horseshoe vortex placed at element j , at control point of element i |
| b | body width, Fig. 13.32 |
| $c_p = \frac{p - p_\infty}{\frac{\rho}{2} V_\infty^2}$ | pressure coefficient |
| grad | gradient (Eqn 13.22) |
| l | body length |
| m, n | number of panels |
| \vec{n} | surface normal vector, Fig. 13.9a |
| p, p_∞ | local and ambient pressure |

| | |
|--------------------------------|---|
| q | a point on body surface |
| r, \vec{r} | radial distance and position vector |
| s | coordinate along body contour, Fig. 13.14 |
| $t, \Delta t$ | time and time interval |
| vol | volume |
| u, v, w | velocity components of vector \vec{V} in x, y and z direction |
| x, y, z | Cartesian coordinates, Fig. 13.1 |
| Γ | vortex strength (Eqn 13.56) |
| θ | polar angle in spherical coordinate system |
| Φ | potential function |
| Ψ | stream function |
| α | angle of incidence |
| β | angle of yaw (angle between direction of motion and wind), Fig. 13.11 |
| δ, δ_1 | boundary layer and displacement thickness |
| δp | pressure change |
| δvol | volume of an element ($= dx dy dz$); also change in volume |
| $\delta \rho$ | change in density |
| μ | viscosity; also local strength of doublet sheet |
| $\nu = \frac{\mu}{\rho}$ | kinematic viscosity |
| ρ | density |
| σ | local strength of source/sink distribution |
| τ | shear stress (Eqn 13.5) |
| φ | cone angle in spherical coordinates; also potential function |
| $\varphi(Q)$ | potential at point Q due to source/sink distribution on body surface |
| $\varphi_D(Q)$ | potential at point Q due to doublet distribution on wake surface |
| $\vec{\omega}$ | vorticity vector $= i\omega_x + j\omega_y + k\omega_z$ |
| $\omega_x, \omega_y, \omega_z$ | components of vorticity vector |
| ∇^2 | Laplace operator (Eqn 13.25) |